J. Mech. Phys. Solids 172 (2023) 105178

Contents lists available at ScienceDirect

Journal of the Mechanics and Physics of Solids

journal homepage: www.elsevier.com/locate/jmps

A continuum theory of organic mixed ionic-electronic conductors of phase separation

Xiaokang Wang, Kejie Zhao *

School of Mechanical Engineering, Purdue University, West Lafayette, IN 47907, United States

ARTICLE INFO

Keywords:
Phase separation
Swelling
Organic mixed ionic-electronic conductors
Organic electrochemical transistors
Multiphysics

ABSTRACT

Organic mixed ionic-electronic conductors (OMIECs) are the core functioning component in the emerging flexible, bio-, and optoelectronics owning to their unique capability of mixed conduction. Of all types, two-phase OMIECs exhibit exceptional performance due to their high stretchability and balanced ionic-electronic conduction. However, the electron-conducting phase may segregate from the ion-conducting phase in a two-phase OMIEC, changing the conducting path and eventually leading to degraded performance and dysfunction of the devices. In this work, we formulate a continuum theory following the thermodynamics framework of a two-phase OMIEC undergoing phase separation. The free energy consists of contributions from the deformation of the polymer chains, the mixing of the polymer with salts and solvents, the electrostatic field, and the two-phase interfaces. The equilibrium conditions and kinetics equations are derived with the constraint of mass conservation, thermodynamics laws, and electrostatics. We implement the theory into a finite element model and study the mechanics and electrochemistry of the OMIEC channel in an electrolyte-gated organic electrochemical transistor (OECT) device. The computational model captures the concurrent transport of charge carriers, mechanical swelling, and phase separation in the OMIEC and replicates the transfer curves of an OECT which agree well with the experiments. More specifically, we reveal the origin of the volumetric capacitance as the accumulation of charge carriers at the two-phase interfaces. We examine the parametric space to elucidate experimental observations such as molecular size-dependent conductivity and substrate-dependent phase separation. The swelling behavior and the transfer curves of OECTs under stretched, free, and constrained states are compared, demonstrating the effects of deformation on the phase dynamics and the electron-conducting behavior. We show that, for volumetric swelling and the electrochemical transfer curves, the effect of stress-transport coupling dominates while the effect of the Maxwell stress is negligible. This work provides a theoretical basis for the mechanics and electrochemistry of two-phase OMIECs.

1. Introduction

Organic mixed ionic-electronic conductors (OMIECs) are a family of materials that enable both ionic and electronic conduction at low bias voltages (< 1 V) (Riess, 2000; Paulsen et al., 2020, 2021; Tan et al., 2022; Kousseff et al., 2022). The bias voltage controls the charge carrier concentration inside the OMIEC, which provides a means for fine control of its doping and conduction states. When a

* Corresponding author.
E-mail address: kjzhao@purdue.edu (K. Zhao).

https://doi.org/10.1016/j.jmps.2022.105178
Received 25 October 2022; Received in revised form 9 December 2022; Accepted 10 December 2022
Available online 15 December 2022
0022-5096/© 2022 Elsevier Ltd. All rights reserved.

Nomenclature

$U^{\mathrm{M}}, U^{\mathrm{C}}, U^{\mathrm{E}}, U^{\mathrm{pf}}$	Work due to mechanical, chemical, electrical, and phase field
$B_i,\ T_i$	Body force, surface traction
μ^m	Chemical (electrochemical) potential of species m
r^m	Source intensity of species m
j^m	Flux of species m
V	Electrostatic potential
F	Faraday constant
$\boldsymbol{F},\ \boldsymbol{F}^{\mathrm{el}},\ \boldsymbol{F}^{\mathrm{inel}}, \boldsymbol{F}^{\mathrm{C}}, \boldsymbol{F}^{\mathrm{pl}}$	Deformation gradient and its elastic, inelastic, chemical, plastic components
$\boldsymbol{\varepsilon}$	Green-Lagrangian strain
$\boldsymbol{C}$	Right Cauchy-Green deformation tensor
$C^{\mathrm{s}},\ C^{\mathrm{c}},\ C^{\mathrm{a}},\ C^{\mathrm{h}}$	Concentration of solvents, cations, anions, and holes
ϕ	Phase parameter (the volume fraction) of phase I
Λ	Determinant of $\boldsymbol{F}^{\mathrm{C}}$
N_K	K-th component of the outward normal vector on the surface
Q	Space charge density
z^m	Valence of charged species m
$\widetilde{D}_K$	K-th component of the nominal electrical displacement
$P,\ \sigma,\ \sigma^{\mathrm{m}}$	First Piola-Kirchhoff stress, Cauchy stress, and mean stress
$W, W^{\mathrm{e}}, W^{\mathrm{pf}}, W^m, W^{\mathrm{s}}, W^{\mathrm{h}}, W^{\mathrm{E}}$	Total free energy and contributions from the strain, phase field, mobile ions, solvent, hole, and the electrical field
$\boldsymbol{F}^{-\mathrm{pl}}$	Inverse of $\boldsymbol{F}^{\mathrm{pl}}$
F^{y}	Yield Function
G, λ	Lamé constants
$I_1(C^{\mathrm{el}})$	First invariant of the elastic component of the right Cauchy-Green tensor
J^{el}	Determinant of the elastic deformation gradient
f^0	Free energy of the two unmixed phases
$\mu^{i,0},\ N^i$	Chemical potential and number of monomers per chain in phase i
$\chi^m,\ \chi^\phi$	Flory parameter of mixing for mobile species m in OMIEC and the two OMIEC phases
κ	Coefficient of the interfacial energy
a	Characteristic chain length
$\Delta\gamma$	Difference of the interfacial energy $\gamma_{\mathrm{PEDOT-substrate}} - \gamma_{\mathrm{PSS-substrate}}$
ρ^{sub}	Molar density of the substrate
$w(X_2), d$	Interaction potential and interaction length between the substrate and the OMIEC
v^m	Molecular volume of the species m
ε	Dielectric constant
l, h, w	Length, thickness, and width of the OMIEC channel in the OECT

positive voltage is applied, electrons leave the OMIEC, and anions are injected to maintain electroneutrality. This doping process increases the conductivity of OMIECs by several orders of magnitude (Das et al., 2020). Conversely, a negative voltage reverts the charge carriers and deprives the high electronic conductivity.

The mixed conduction of ionic and electronic charge carriers makes OMIECs-based devices ideal for sensing (Nambiar and Yeow, 2011; Picca et al., 2020), information processing (Gkoupidenis et al., 2015; Yamamoto et al., 2022), energy storage (Olmo et al., 2022), electrochromics (Li et al., 2019), and bioelectronics (Zhang et al., 2022). For instance, OMIECs can be utilized as the channel material in organic electrochemical transistors (OECTs), as sketched in Fig. 1 (Rivnay et al., 2018; Hidalgo Castillo et al., 2022). In an OECT, there is a gate electrode immersed in the electrolyte, a source electrode, and a drain electrode connected to the source by the OMIEC channel. The gate voltage dictates the conduction state of the OMIEC channel, and the drain voltage provides a bias for current flow from the source electrode. When a proper gate voltage is applied against the grounded source electrode, the OMIEC channel is doped with a high electronic conductivity, which turns the transistor on and allows large current drainage. Conversely, a reverse voltage at the gate electrode turns the transistor off. The fast-responding, low-power-consuming, and biocompatible OECTs can be used in wearable sensors for sweat monitoring (Aerathupalathu Janardhanan et al., 2022) and brain-machine interfaces for transmitting and accepting neuron signals (Liang et al., 2021; Go et al., 2022).

The dynamics of OMIECs during electrochemical processes need to be understood from both the mechanical and electrochemical

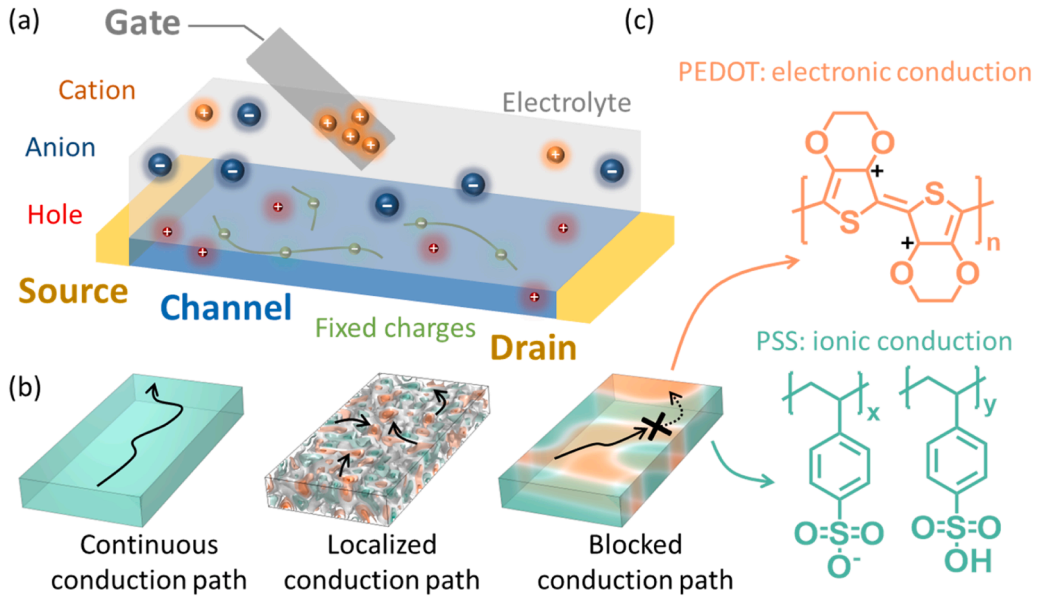

Fig. 1. Two-phase OMIECs as the channel material in organic electrochemical transistors. (a) Sketch of an OECT with holes (red) and fixed negative charges (green) in the channel immersed in the electrolyte with cations (orange) and anions (blue). (b) Sketch of the phase separation and evolution of the conducting pathway. (c) Molecular structure of a representative OMIEC, PEDOT:PSS.

perspectives. In contact with an electrolyte, the OMIECs absorb solvents and ions due to the gradient of their chemical potentials and swell in the volume. The solution thermodynamics and mechanical swelling have been well studied since Gibbs (Gibbs, 1878; Flory and Rehner, 1943; Tanaka and Fillmore, 1979; Shibayama and Tanaka, 1993; Hong et al., 2008; Zhang et al., 2020; Bosnjak et al., 2022). The electrochemical aspect of OMIECs adds the motion of ions and electrons in the existing theories. The electronic conducting path in OMIECs is determined by the phase structure. In a single-phase OMIEC, the charge carriers may flow along a continuous electron-conducting path. Nevertheless, high-performance OMIECs are often mixtures of ion-conducting and electron-conducting phases with balanced ionic and electronic conduction (Keene et al., 2022). In two-phase stretchable OMIECs (Kayser and Lipomi, 2019), the transport of electronic charge carriers is fulfilled by hopping/tunneling along the tortuous electronically conductive phase (Honma et al., 2018; Gueye et al., 2020), as illustrated in Fig. 1(b). Recent studies on conducting polymer blends have shown that long-range tunneling between isolated electron-conducting phases is limited to ~ 3 nm (Keene et al., 2022; Makki and Troisi, 2022). As an example, poly(3,4-ethylenedioxythiophene) polystyrene sulfonate (PEDOT:PSS, Fig. 1(c)) is one of the best-performing two-phase OMIECs which consists of the electronically conductive (via hole) PEDOT phase and the negatively charged PSS phase (Shi et al., 2015; Kayser and Lipomi, 2019; Dingler et al., 2022). During the doping process, holes are injected into PEDOT and cations are expulsed from the negatively charged PSS phase. In the exercise of doping and dedoping, PEDOT:PSS films often experience phase separation either horizontally in the plane or vertically through the thickness direction, as shown in Fig. S1, especially when polar solvents are added to further improve the conductivity (Cruz-Cruz et al., 2010; Yeo et al., 2012; Ouyang et al., 2015; Yildirim et al., 2018). As a result, the large-scale phase separation in OMIECs can block the conducting path and cause the breakdown of the mixed conduction.

Phase separation of OMIECs is a challenging subject in phase field modeling such as on polymeric gels which swell to coexisting states of different concentrations of guest species (Shibayama and Tanaka, 1993; Cai and Suo, 2011; Hong and Wang, 2013; Zhao et al., 2016; Yu et al., 2017; Celora et al., 2022). Gels are typically regarded as a single molecular network with collective diffusion characteristics that the material particles do not change their relative positions (Shibayama and Tanaka, 1993). In gel swelling, the concentration of guest species delineates different states. However, for the OMIECs undergoing phase separation, it is the concentration of a certain host molecule that determines the phases. For example, the phases in PEDOT:PSS are not dictated by the solvent concentration but by the concentration of the PEDOT molecules. This feature calls for caution in the direct use of the aforementioned theories proposed for crosslinked polymeric gels, because the relative positions of the material particles in two-phase OMIECs may not be preserved during the large-scale phase separation. Nevertheless, previous studies pointed out that this problem can be partially circumvented for host materials that preserve the relative positions for at least some material particles (Hong and Wang, 2013; Kim et al., 2022).

The modeling of electrochemistry in OMIECs presents another challenge. The first hurdle is the determination of the electrochemical potential of the electronic charge carriers, which involves assumptions of the electronic density of states (Tybrandt et al.,

2017). The second challenge is the determination of the spatial distribution of the ionic and electronic carriers and the precise description of their interactions. One lasting question is whether local electroneutrality breaks down. Wang et al. (2009) distinguished two cases for Poisson's electrostatic equation: idealized electroneutrality where the space charge density is strictly set to zero versus limited electroneutrality where the space charge is determined by the local concentration of charge carriers. They concluded that for charge transport behaviors, the condition of electroneutrality makes little difference. In another study, Celora et al. (2022) showed that the breakdown of local electroneutrality leads to a new mode of phase instability in polyelectrolyte gels when the Kuhn length is comparable with the Debye length. In PEDOT:PSS of large-scale phase separation, the negative charges in the PSS phase and the positive charges in PEDOT could cause a violation of electroneutrality of each phase without the compensated charge carriers. Therefore, it is necessary to determine the carrier distributions in OMIECs to understand their electrochemical behaviors. Thirdly, the majority of previous studies on the electrochemical performance of two-phase OMIECs utilize homogeneous single-phase models which do not distinguish the electron-conducting and ion-conducting phases. Volkov et al. (2017) used a simplified sandwich structure of PSS-PEDOT-PSS and captured the capacitive current that is entirely missing in the single-phase models. Despite this success, a more accurate model that can describe the realistic phase structures of two-phase OMIECs is urgently needed.

In this work, we propose a continuum theory of a two-phase OMIEC of phase separation following the thermodynamics framework and derive the governing equations for the equilibrium and kinetic processes. Using free energy consisting of the deformation of polymer chains, the mixing of solvent and salts with polymers, the two-phase interfaces, and the electrostatic field, we derive the constitutive relations. We implement the theory into a finite element model and study the mechanics, electrochemistry, and their coupling in OMIECs. We examine the material parameter space and identify the conditions that well capture experimental observations such as mechanical swelling and phase separation in a two-phase OMIEC, and furthermore the transfer curves of an OECT device. We evaluate the evolution of the conducting path and the transfer curves in stretched, free, and constrained OECTs as the OMIEC phases segregate. We also compare the effects of the transport-stress coupling versus the Maxwell stress on the transfer curves of an OECT and find that in such cases the Maxwell stress can be neglected. This work provides a theoretical basis for understanding the mechanics and electrochemistry of the state-of-the-art two-phase OMIECs.

2. Theory

2.1. Thermodynamics, mass conservation, and electrostatics

We follow the Coleman-Noll procedure (Coleman and Noll, 1963; Truesdell and Noll, 2004), which applied the general principles and material-specific assumptions in an elegant and unified mathematical description, to formulate the theory. In the continuum theory, we assume that the relative positions of at least some material particles are preserved during the phase separation, which allows us to track the deformation during the evolution process. Following a prior work on polymeric gels by Hong et al. (2008, 2010), we consider a system connected to a pump with constant chemical potential μ^m of mobile species m, a pump with constant chemical potential μ^ϕ of phase ϕ, a battery with constant electrical potential V, and a weight with constant pressure. In the current state, the mechanical work due to infinitesimal changes in displacement δx_i of the material particle $\boldsymbol{X}(\boldsymbol{X}, t)$ is

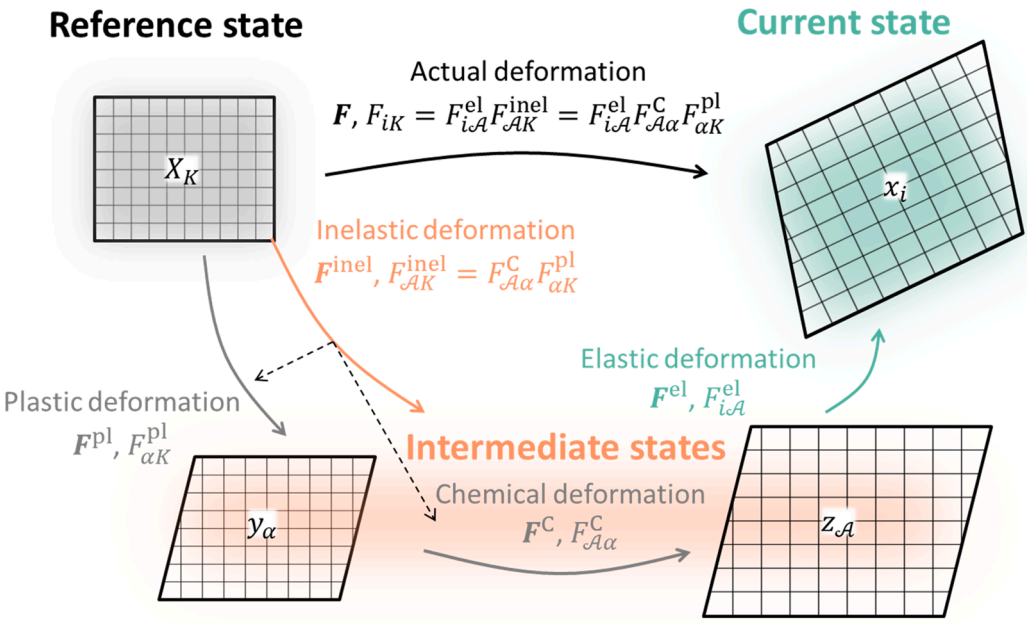

Fig. 2. Multiplicative decomposition of the deformation gradient tensor at each material particle.

$$\delta U^{\mathrm{M}} = \int_{\Omega} B_i(\boldsymbol{X},t)\delta x_i \mathrm{d}\Omega + \int_{S} T_i(\boldsymbol{X},t)\delta x_i \mathrm{d}S, \tag{1}$$

where $B_i(\boldsymbol{X},t)$ is the body force density and $T_i(\boldsymbol{X},t)$ is the surface force density. The chemical work due to infinitesimal changes in the number of the mobile species m is

$$\delta U^{\mathrm{C}} = \sum_m \int_{\Omega} \mu^m(\boldsymbol{X},t)\delta r^m \mathrm{d}\Omega + \sum_m \int_{S} \mu^m(\boldsymbol{X},t) j^m \delta t \mathrm{d}S, \tag{2}$$

where r^m is the source intensity, and j^m is the surface flux. The superscript m represents one of the following mobile species: solvent, anion, cation, and hole. The electric work due to infinitesimal changes in the number of holes is

$$\delta U^{\mathrm{E}} = \int_{\Omega} FV(\boldsymbol{X},t)\delta r^{\mathrm{h}} \mathrm{d}\Omega + \int_{S} FV(\boldsymbol{X},t) j^{\mathrm{h}} \delta t \mathrm{d}S, \tag{3}$$

where F is the Faraday constant, r^{h} is the source intensity, and j^{h} is the surface flux. For a two-phase OMIEC, we define the volume fraction of phase I as the phase parameter ϕ, and the volume fraction of phase II is $1-\phi$. For example, in the blend of PEDOT:PSS polymers, the volume fraction is related to the concentration of the monomer EDOT in the PEDOT phase by $\phi = \frac{C^{\mathrm{EDOT}}}{C^{\max}} = C^{\mathrm{EDOT}} v^{\mathrm{EDOT}}$, where v^{EDOT} is the volume of the EDOT monomer. The work due to infinitesimal changes in the phase parameter ϕ is

$$\delta U^{\mathrm{pf}} = \int_{\Omega} \mu^{\phi}(\boldsymbol{X},t)\delta r^{\phi} \mathrm{d}\Omega + \int_{S} \mu^{\phi}(\boldsymbol{X},t) j^{\phi} \delta t \mathrm{d}S, \tag{4}$$

where r^{ϕ} is the source intensity, and j^{ϕ} is the surface flux.

The material particle $\boldsymbol{X}$ in the reference configuration resides at $\boldsymbol{x}$ in the current configuration. Define the deformation gradient F_{iK} as

$$F_{iK} = \frac{\partial x_i}{\partial X_K}. \tag{5}$$

As illustrated in Fig. 2, the deformation gradient is multiplicatively decomposed into an elastic component $\boldsymbol{F}^{\mathrm{el}}$ and an inelastic part $\boldsymbol{F}^{\mathrm{inel}}$ as follows (Simo and Hughes, 2006),

$$F_{iK} = F^{\mathrm{el}}_{i\mathscr{A}} F^{\mathrm{inel}}_{\mathscr{A}K} = F^{\mathrm{el}}_{i\mathscr{A}} F^{\mathrm{C}}_{\mathscr{A}\alpha} F^{\mathrm{pl}}_{\alpha K}, \tag{6}$$

where $F^{\mathrm{C}}_{\mathscr{A}\alpha}$ represents the deformation due to the insertion of the mobile species, and $F^{\mathrm{pl}}_{\alpha K}$ represents the plastic deformation.

The elastic strain is defined by the elastic component of the right Cauchy-Green deformation tensor $C^{\mathrm{el}}_{\mathscr{A}\mathscr{B}} = F^{\mathrm{el}}_{i\mathscr{A}} F^{\mathrm{el}}_{i\mathscr{B}}$ as

$$\varepsilon^{\mathrm{el}}_{\mathscr{A}\mathscr{B}} = \frac{1}{2}\left(C^{\mathrm{el}}_{\mathscr{A}\mathscr{B}} - \delta_{\mathscr{A}\mathscr{B}}\right) = \frac{1}{2}\left(F^{\mathrm{el}}_{i\mathscr{A}} F^{\mathrm{el}}_{i\mathscr{B}} - \delta_{\mathscr{A}\mathscr{B}}\right). \tag{7}$$

Assuming incompressibility it yields (Zhao et al., 2011)

$$\det\left(\boldsymbol{F}^{\mathrm{C}}\right) = \Lambda = \Lambda(C^{\mathrm{s}},\ C^{\mathrm{c}},\ C^{\mathrm{a}}) = 1 + \sum_m C^m v^m, \tag{8}$$

where v^m is the volume of the mobile species, and C^{s}, C^{c}, C^{a} represent the solvent concentration, cation concentration, and anion concentration in the OMIECs, respectively. Assuming isotropic deformation of the host upon the insertion of the mobile species, one has

$$F^{\mathrm{C}}_{\mathscr{A}\alpha} = \Lambda^{\frac{1}{3}} \delta_{\mathscr{A}\alpha} \tag{9}$$

The conservation of all species, including the solvent, charge carriers, and matrix molecules, is given by

$$C^m(\boldsymbol{X}, t+\delta t) - C^m(\boldsymbol{X},\ t) + \frac{\partial J^m_K(\boldsymbol{X},t)}{\partial X_K}\delta t = r^m(\boldsymbol{X},\ t), \tag{10a}$$

in the volume and

$$N_K\left[J_K^m(\boldsymbol{X},t)\right]^+ - N_K\left[J_K^m(\boldsymbol{X},t)\right]^- = j^m(\boldsymbol{X},t), \tag{10b}$$

on the surface, where C^m is the concentration of individual mobile species m, and N_K is the surface normal. The superscript "+" ("–") represents the value of the quantity at the outward (inward) side of the surface. In particular, the conservation of the host molecule (phase parameter ϕ) in the volume is given by

$$\phi(\boldsymbol{X},t+\delta t) - \phi(\boldsymbol{X},\ t) + \frac{\partial J_K^{\phi}(\boldsymbol{X},\ t)}{\partial X_K}\delta t = 0. \tag{11}$$

The space charge density Q is given by

$$Q = \left(r^{\mathrm{h}} + \sum_m z^m C^m + z^0 C^0\right)F, \tag{12}$$

where r^{h} is the number of injected holes, z^m is the charge per mobile species, z^0 and C^0 are the valence and concentration of the fixed charges. For solvent, $z^{\mathrm{s}} = 0$. For simplicity, we take $z^{\mathrm{c}} = z^{\mathrm{h}} = 1$ and $z^{\mathrm{a}} = -1$. The Poisson's equation is

$$\frac{\partial \widetilde{D}_K(\boldsymbol{X},t)}{\partial X_K} = Q(\boldsymbol{X},t), \tag{13a}$$

in the volume and

$$N_K[\widetilde{D}_K(\boldsymbol{X},t)]^+ - N_K[\widetilde{D}_K(\boldsymbol{X},t)]^- = Fj^{\mathrm{h}}(\boldsymbol{X},t)\delta t, \tag{13b}$$

on the surface, where $\widetilde{D}_K(\boldsymbol{X},t)$ is the electrical displacement.

Consider the free energy as a function of the elastic deformation, electrical displacement, concentration of all species, phase parameter, and the gradient of the phase parameter, $W = W(\boldsymbol{\varepsilon}^{\mathrm{el}},\widetilde{\boldsymbol{D}},C^m,\phi,\nabla\phi\ )$. We take the variation of the free energy as the change of the free energy related to the infinitesimally small changes,

$$\delta W\left(\boldsymbol{\varepsilon}^{\mathrm{el}},\widetilde{\boldsymbol{D}},C^m,\phi,\nabla\phi\ \right) = \frac{\partial W}{\partial \varepsilon^{\mathrm{el}}_{\mathscr{A}\mathscr{B}}}\delta\varepsilon^{\mathrm{el}}_{\mathscr{A}\mathscr{B}} + \frac{\partial W}{\partial \widetilde{D}_K}\delta\widetilde{D}_K + \sum_m \frac{\partial W}{\partial C^m}\delta C^m + \frac{\partial W}{\partial \phi}\delta\phi + \frac{\partial W}{\partial(\nabla\phi)_K}\delta(\nabla\phi)_K \tag{14}$$

Note that C^m in Eq. (14) also includes C^{h}. The second law of thermodynamics requires that

$$\int_\Omega \delta W - \left(\delta U^{\mathrm{M}} + \delta U^{\mathrm{C}} + \delta U^{\mathrm{E}} + \delta U^{\mathrm{pf}}\right)\mathrm{d}\Omega \le 0. \tag{15}$$

2.2. Governing equations

Using Eqs. (1)–(14), (15) is expanded as follows. The detailed derivation is attached in Appendix A.

$$\int_\Omega \delta W - \left(\delta U^{\mathrm{M}} + \delta U^{\mathrm{C}} + \delta U^{\mathrm{E}} + \delta U^{\mathrm{pf}}\right)\mathrm{d}\Omega = T^{\mathrm{M}} + T^{\mathrm{C}} + T^{\mathrm{E}} + T^{\mathrm{pf}} \le 0, \tag{16}$$

where

$$\begin{aligned} T^{\mathrm{M}} \quad = \quad & -\int_\Omega \delta x_i\left[\frac{\partial}{\partial X_K}\left(\frac{\partial W}{\partial \varepsilon^{\mathrm{el}}_{\mathscr{A}\mathscr{B}}}F^{\mathrm{el}}_{i\mathscr{A}}F^{-\mathrm{pl}}_{K\beta}F^{-\mathrm{C}}_{\beta\mathscr{B}}\right) + B_i\right]\mathrm{d}\Omega \\ & -\int_S\left[N_K\left(\frac{\partial W}{\partial \varepsilon^{\mathrm{el}}_{\mathscr{A}\mathscr{B}}}F^{\mathrm{el}}_{i\mathscr{A}}F^{-\mathrm{pl}}_{K\beta}F^{-\mathrm{C}}_{\beta\mathscr{B}}\delta x_i\right)^+ - N_K\left(\frac{\partial W}{\partial \varepsilon^{\mathrm{el}}_{\mathscr{A}\mathscr{B}}}F^{\mathrm{el}}_{i\mathscr{A}}F^{-\mathrm{pl}}_{K\beta}F^{-\mathrm{C}}_{\beta\mathscr{B}}\delta x_i\right)^- + T_i\delta x_i\right]\mathrm{d}S \\ & +\int_\Omega \frac{\partial W}{\partial \varepsilon^{\mathrm{el}}_{\mathscr{A}\mathscr{B}}}F^{\mathrm{el}}_{i\mathscr{A}}F_{i\mathrm{K}}F^{-\mathrm{C}}_{\beta\mathscr{B}}\delta\left(F^{-\mathrm{pl}}_{K\beta}\right)\mathrm{d}\Omega, \end{aligned} \tag{16a}$$

$$
\begin{aligned}
T^{\mathrm{C}} = & \sum_{m\neq h}\int_{\Omega}\frac{\partial W}{\partial C^m}+FVz^m-\frac{1}{3}\frac{\partial W}{\partial \varepsilon^{\mathrm{el}}_{\mathscr{A}\mathscr{B}}}F^{\mathrm{el}}_{i\mathscr{A}}F^{\mathrm{el}}_{i\mathscr{B}}\frac{1}{\Lambda}\frac{\partial \Lambda}{\partial C^m}-\mu^m\delta r^m\mathrm{d}\Omega \\
& +\sum_{m\neq h}\int_{\Omega}J^m_L\delta t\frac{\partial}{\partial X_L}\left(\frac{\partial W}{\partial C^m}+FVz^m-\frac{1}{3}\frac{\partial W}{\partial \varepsilon^{\mathrm{el}}_{\mathscr{A}\mathscr{B}}}F^{\mathrm{el}}_{i\mathscr{A}}F^{\mathrm{el}}_{i\mathscr{B}}\frac{1}{\Lambda}\frac{\partial \Lambda}{\partial C^m}\right)\mathrm{d}\Omega \\
& +\sum_{m\neq h}\int_{S}N_L\left(J^m_L\delta t\right)^{+}\left(\frac{\partial W}{\partial C^m}+FVz^m-\frac{1}{3}\frac{\partial W}{\partial \varepsilon^{\mathrm{el}}_{\mathscr{A}\mathscr{B}}}F^{\mathrm{el}}_{i\mathscr{A}}F^{\mathrm{el}}_{i\mathscr{B}}\frac{1}{\Lambda}\frac{\partial \Lambda}{\partial C^m}-\mu^m\right)^{+}\mathrm{d}S \\
& -\sum_{m\neq h}\int_{S}N_L\left(J^m_L\delta t\right)^{-}\left(\frac{\partial W}{\partial C^m}+FVz^m-\frac{1}{3}\frac{\partial W}{\partial \varepsilon^{\mathrm{el}}_{\mathscr{A}\mathscr{B}}}F^{\mathrm{el}}_{i\mathscr{A}}F^{\mathrm{el}}_{i\mathscr{B}}\frac{1}{\Lambda}\frac{\partial \Lambda}{\partial C^m}-\mu^m\right)^{-}\mathrm{d}S \\
& +\int_{\Omega}\frac{\partial W}{\partial C^h}+FV-\mu^h\delta r^h\mathrm{d}\Omega+\int_{\Omega}J^{\mathrm{h}}_L\delta t\frac{\partial}{\partial X_L}\left(\frac{\partial W}{\partial C^h}+FV-\mu^h\right)\mathrm{d}\Omega \\
& +\int_{S}\left[\left(\frac{\partial W}{\partial C^h}+FV-\mu^h\right)^{+}\left(J^{\mathrm{h}}_L\delta t\right)^{+}-\left(\frac{\partial W}{\partial C^h}+FV-\mu^h\right)^{-}\left(J^{\mathrm{h}}_L\delta t\right)^{-}\right]N_K\mathrm{d}S
\end{aligned}
\tag{16b}
$$

$$
T^{\mathrm{E}}=\int_{\Omega}\left(\frac{\partial W}{\partial \widetilde{D}_K}+\frac{\partial V}{\partial X_K}\right)\delta\widetilde{D}_K\mathrm{d}\Omega+\int_{S}(\delta\widetilde{D}_KV)^{+}N_K-(\delta\widetilde{D}_KV)^{-}N_K\mathrm{d}S, \tag{16c}
$$

$$
\begin{aligned}
T^{\mathrm{pf}} = & \int_{\Omega}\left(\frac{\partial W}{\partial \phi}-\frac{\partial}{\partial X_K}\frac{\partial W}{\partial(\nabla\phi)_K}-\mu^{\phi}\right)\delta r^{\phi}\mathrm{d}\Omega+\int_{\Omega}J^{\phi}_L\delta t\frac{\partial}{\partial X_L}\left(\frac{\partial W}{\partial \phi}-\frac{\partial}{\partial X_K}\frac{\partial W}{\partial(\nabla\phi)_K}\right)\mathrm{d}\Omega \\
& -\int_{S}\left[\left(\frac{\partial W}{\partial \phi}-\frac{\partial}{\partial X_K}\frac{\partial W}{\partial(\nabla\phi)_K}-\mu^{\phi}\right)J^{\phi}_L\delta t\right]^{-}N_L-\left[\left(\frac{\partial W}{\partial \phi}-\frac{\partial}{\partial X_K}\frac{\partial W}{\partial(\nabla\phi)_K}-\mu^{\phi}\right)J^{\phi}_L\delta t\right]^{+}N_L\mathrm{d}S \\
& +\int_{S}\left[N_K\left(\frac{\partial W}{\partial(\nabla\phi)_K}\right)^{-}-N_K\left(\frac{\partial W}{\partial(\nabla\phi)_K}\right)^{+}\right]\delta\phi\mathrm{d}S
\end{aligned}
\tag{16d}
$$

Note that $\boldsymbol{F}^{-\mathrm{pl}}$ represents the inverse of $\boldsymbol{F}^{\mathrm{pl}}$, and $\boldsymbol{F}^{-\mathrm{C}}=\Lambda^{-\frac{1}{3}}\boldsymbol{I}$ is the inverse of $\boldsymbol{F}^{\mathrm{C}}$. Each of the terms in Eq. (16) governs a unique process. Only when the system is at equilibrium, the equality holds. Inequality holds due to the inelastic deformation of the host materials, the kinetics of mass transport, and the irreversible phase separation which make the increase in free energy less than the work done to the system.

We shall now examine each of the terms in Eq. (16) and reveal their significance. Intensive quantities are defined to denote the governing equations for the equilibrium state and kinetic processes. T^{M} in Eq. (16) describes the mechanical processes. To ensure that the sum is no greater than zero for all admissible δx_i, the coefficients in the first two terms in T^{M} must vanish. Define the first Piola-Kirchhoff stress and Cauchy stress as follows.

$$
P_{iK}=\frac{\partial W}{\partial \varepsilon^{\mathrm{el}}_{\mathscr{A}\mathscr{B}}}F^{\mathrm{el}}_{i\mathscr{A}}F^{-\mathrm{pl}}_{K\beta}F^{-\mathrm{C}}_{\beta\mathscr{B}}, \tag{17a}
$$

$$
\sigma_{ij}=\frac{1}{\det(\boldsymbol{F})}P_{iK}F_{jK}. \tag{17b}
$$

Then, the first two terms in T^{M} yield mechanical equilibrium in the volume and on the surface in the reference configuration,

$$
\frac{\partial P_{iK}}{\partial X_K}+B_i=0, \tag{18a}
$$

$$
T_i+N_K(P_{iK})^{+}-N_K(P_{iK})^{-}=0. \tag{18b}
$$

Note that we recovered the classical mechanical equilibrium equation and the traction boundary condition. The third term in T^{M} describes the plastic dissipation. Using Eqs. (6) and (18),

$$
\int_{\Omega}\frac{\partial W}{\partial \varepsilon^{\mathrm{el}}_{\mathscr{A}\mathscr{B}}}F^{\mathrm{el}}_{i\mathscr{A}}F_{iK}F^{-\mathrm{C}}_{\beta\mathscr{B}}\delta\left(F^{-\mathrm{pl}}_{K\beta}\right)\mathrm{d}\Omega=\int_{\Omega}P_{iL}F^{\mathrm{pl}}_{\beta L}F_{iK}\delta\left(F^{-\mathrm{pl}}_{K\beta}\right)\mathrm{d}\Omega=\int_{\Omega}\Sigma_{KL}F^{\mathrm{pl}}_{\beta L}\delta\left(F^{-\mathrm{pl}}_{K\beta}\right)\mathrm{d}\Omega=-\int_{\Omega}\Sigma_{KL}F^{-\mathrm{pl}}_{K\beta}\delta\left(F^{\mathrm{pl}}_{\beta L}\right)\mathrm{d}\Omega, \tag{19}
$$

where $\Sigma_{KL}=P_{iL}F_{iK}$ is the Mandel stress (Lubliner, 2008). To enforce inequality, the flow rule must satisfy the following,

$$
\Sigma_{KL}F^{-\mathrm{pl}}_{K\beta}\dot{F}^{\mathrm{pl}}_{\beta L}\geq 0. \tag{20}
$$

As an example, we choose the associated plastic flow rule as follows (Anand et al., 2012; Di Leo et al., 2015),

$$F^{-\mathrm{pl}}_{K\beta}\dot{F}^{\mathrm{pl}}_{\beta L} = \mathscr{H}\frac{\partial F_{\mathrm{y}}}{\partial \Sigma_{KL}}, \tag{21a}$$

where the plastic multiplier and the yield function satisfy the Kuhn-Tucker conditions (Simo, 1992; Simo and Hughes, 2006),

$$\mathscr{H} \geq 0,\ F_{\mathrm{y}} \leq 0,\ \mathscr{H}F_{\mathrm{y}} = 0. \tag{21b}$$

The yield function for plastic deformation is written in terms of the yield stress σ^{y} and the deviatoric part of Σ^{d} as

$$F^{\mathrm{y}} = \sqrt{\frac{3}{2}\Sigma^{\mathrm{d}}_{KL}\Sigma^{\mathrm{d}}_{KL}} - \sigma^{\mathrm{y}}. \tag{21c}$$

The terms in T^{C} in Eq. (16) describe the transport of all mobile species. From Eq. (17b), the mean stress σ^{m} can be defined as follows.

$$\sigma^{\mathrm{m}} = \frac{1}{3}\sigma_{kk} = \frac{1}{3}\frac{1}{\det(\boldsymbol{F})}\frac{\partial W}{\partial e^{\mathrm{el}}_{\mathscr{A}\mathscr{B}}}F^{\mathrm{el}}_{i\mathscr{A}}F^{-\mathrm{pl}}_{K\beta}F^{-\mathrm{C}}_{\beta\mathscr{B}}F_{iK} = \frac{1}{3}\frac{1}{\det(\boldsymbol{F})}\frac{\partial W}{\partial e^{\mathrm{el}}_{\mathscr{A}\mathscr{B}}}F^{\mathrm{el}}_{i\mathscr{A}}F^{\mathrm{el}}_{i\mathscr{B}}. \tag{22}$$

Define the partial molar volume of a mobile species in a stressed solid as follows,

$$v^m = \frac{\det(\boldsymbol{F})}{\Lambda}\frac{\mathrm{d}\Lambda}{\mathrm{d}C^m}. \tag{23}$$

Then, the electrochemical potential of the mobile species is defined as follows to satisfy the inequality for all admissible δr^m,

$$\mu^m = \frac{\partial W}{\partial C^m} + FVz^m - \sigma^{\mathrm{m}}v^m, \tag{24a}$$

$$\mu^{\mathrm{h}} = \frac{\partial W}{\partial C^{\mathrm{h}}} + FV. \tag{24b}$$

Now, the only non-vanishing terms are the volume integral on the flux. To maintain the inequality for all possible δJ^m_K, the following kinetics equations are chosen for convenience,

$$J^m_L = -\mathscr{M}^m_{LK}\frac{\partial \mu^m}{\partial X_K}, \tag{25a}$$

$$J^{\mathrm{h}}_L = -\mathscr{M}^{\mathrm{h}}_{LK}\frac{\partial \mu^{\mathrm{h}}}{\partial X_K}, \tag{25b}$$

where $\mathscr{M}$ is the mobility of the mobile species.

The terms in T^{E} in Eq. (16) describe the electrostatic field. Define the electrical field as

$$\widetilde{E}_K = \frac{\partial W}{\partial \widetilde{D}_K} = -\frac{\partial V}{\partial X_K}. \tag{26}$$

Since the voltage and electrical displacement evaluated on both sides of the surface are the same, the surface integral vanishes.

The terms in T^{pf} in Eq. (16) describe the phase field in the OMIEC. Similarly, we define the chemical potential of the OMIEC material as

$$\mu^{\phi} = \frac{\partial W}{\partial \phi} - \frac{\partial}{\partial X_K}\frac{\partial W}{\partial (\nabla\phi)_K}. \tag{27}$$

And the inequality is enforced by taking that

$$J^{\phi}_K = -\mathscr{M}^{\phi}\frac{\partial \mu^{\phi}}{\partial X_K}. \tag{28}$$

where $\mathscr{M}^{\phi}$ is the mobility of the OMIEC molecules.

The mobilities of the mobile species and the phase parameter are linked to the diffusivities and deformation gradient as follows (Hong et al., 2008)

$$\mathscr{M}^m_{IJ} = \frac{C^m D^m}{RT}F^{-1}_{Ik}F^{-1}_{Jk} = \frac{C^m D^m}{RT}C^{-1}_{IJ}, \tag{29}$$

where D^m is the diffusivity, R is the gas constant, and T is the temperature.

2.3. Explicit forms of the free energy

The free energy W consists of six components, including contributions from the elastic deformation of the polymer W^{el}, the matrix material and two-phase interfaces W^{pf}, mobile ions W^{m}, solvent W^{s}, holes W^{h}, and the electrical field W^{E}.

$$W = W^{\mathrm{el}} + W^{\mathrm{pf}} + W^{m} + W^{\mathrm{s}} + W^{\mathrm{h}} + W^{\mathrm{E}} \tag{30}$$

Implied by the experimental measurement of the tensile stress-strain curves (Lang et al., 2009), we choose the Neo-Hookean hyperelastic constitutive relation for the elastic deformation and a perfectly plastic model. The elastic free energy is expressed as

$$W^{\mathrm{el}} = \frac{1}{2}G\left[I_1\left(C^{\mathrm{el}}\right) - 3 - 2\ln\left(J^{\mathrm{el}}\right)\right] + \frac{1}{2}\lambda\left[\ln\left(J^{\mathrm{el}}\right)\right]^2. \tag{31}$$

where G and λ are the Lamé constants, I_1 is the first invariant of the elastic component of the right Cauchy-Green deformation tensor C^{el}, and $J^{\mathrm{el}} = \det(\boldsymbol{F}^{\mathrm{el}})$.

Following Cahn and Hilliard (1958), Cahn (1965), and Velázquez Sánchez (2002), we express the free energy of the polymer and the two-phase interfaces in terms of both the phase parameter and its gradient

$$W^{\mathrm{pf}} = f^{0}(\phi) + \kappa(\nabla\phi)^2 + \phi w(X_2). \tag{32}$$

where $f^{0}(\phi)$ is the free energy of the mixture without the interfacial energy, $\kappa(\nabla\phi)^2$ is the excess free energy associated with the interface, and $\phi w(X_2)$ is the interaction energy of the polymer with the substrate. Following Flory (1942), we take

$$f^{0} = \phi\mu^{I,0} + (1-\phi)\mu^{II,0} + RT\left[\frac{\phi}{N^{I}}\ln\phi + \frac{(1-\phi)}{N^{II}}\ln(1-\phi) + \chi^{\phi}\phi(1-\phi)\right]. \tag{33}$$

where $\mu^{i,0}$ and N^{i} are the chemical potential and the number of monomers per chain in the phase I or II, respectively. χ^{ϕ} is the Flory parameter of mixing.

The coefficient κ is related to the interaction length a, χ^{ϕ}, and ϕ by

$$\kappa(\phi) = RTa^2\left(\frac{\chi^{\phi}}{6} + \frac{1}{36\phi(1-\phi)}\right). \tag{34}$$

At a vertical distance of X_2 from the substrate, the coefficient $w(X_2)$ is related to the molar density of the substrate ρ^{sub}, interaction length d, and the difference in the interfacial energies $\Delta\gamma = \gamma_{\mathrm{PEDOT-substrate}} - \gamma_{\mathrm{PSS-substrate}}$ by

$$w(X_2) = -\frac{4\Delta\gamma}{\rho^{\mathrm{sub}}d\left(1 + \frac{X_2}{d}\right)^3} \tag{35}$$

In Flory's theory (Flory, 1942), the free energy of solvent in the electrolyte $W^{s-\mathrm{electrolyte}}$ is expressed in terms of its concentration C^{s} and the molar volume v^{m} as

$$W^{s-\mathrm{electrolyte}} = RTC^{\mathrm{s}}\ln\frac{1}{1 + \sum_{m\neq \mathrm{s}} v^{m}C^{m}}. \tag{36}$$

where m is summed over all ions. Note that we take the assumption that the partial molar volume equals the molar volume. The free energy of each ion in the electrolyte $W^{m-\mathrm{electrolyte}}$ is expressed in terms of its concentration C^{m} and the volume v^{m} as

$$W^{m-\mathrm{electrolyte}} = RT\left\{C^{m}\ln\frac{v^{m}C^{m}}{1 + \sum_{j\neq \mathrm{s}} v^{j}C^{j}}\right\}. \tag{37}$$

Note that we ignored the insignificant enthalpy of mixing in the electrolyte. In the OMIEC, both the salt and the solvents are guest species. The free energy of solvents and ions in OMIEC, $W^{m-\mathrm{OMIEC}}$, is expressed in terms of its concentration C^{m}, the volume v^{m}, and Flory parameter of mixing χ^{m} as

$$W^{m-\mathrm{OMIEC}} = RT\left(C^{m}\ln\frac{v^{m}C^{m}}{1 + \sum_{j} v^{j}C^{j}} + \frac{\chi^{m}C^{m}}{1 + \sum_{j} v^{j}C^{j}}\right). \tag{38}$$

The free energy of holes in OMIEC, W^{h}, is expressed in terms of its concentration C^{h} and the reference concentration C^{h0} as

$$W^{\mathrm{h}} = RTC^{\mathrm{h}}\left(\ln\frac{C^{\mathrm{h}}}{C^{\mathrm{h0}}} - 1\right). \tag{39}$$

We write the free energy associated with electrical polarization as (Xiao and Bhattacharya, 2008; Hong et al., 2010; Mozaffari et al., 2022)

$$W^{\mathrm{E}} = \frac{1}{2\varepsilon}\frac{C_{KL}}{\det \boldsymbol{F}}\widetilde{D}_K\widetilde{D}_L, \tag{40}$$

where ε is the dielectric constant.

With the above free energies, we obtain the constitutive relations for the field variables including the Cauchy stress σ_{ij}, the chemical potential of solvent in the electrolyte $\mu^{s-\mathrm{electrolyte}}$, the electrochemical potential of ions in the electrolyte $\mu^{m-\mathrm{electrolyte}}$, the electrochemical potential of all mobile species in the OMIEC $\mu^{m-\mathrm{OMIEC}}$, and the chemical potential μ^{ϕ} of the phase ϕ as follows. The derivation of Eq. (41) is shown in Appendix B.

$$\sigma_{ij} = \frac{1}{\det(\boldsymbol{F})}\left[2G\varepsilon_{ij}^{\mathrm{el}} + \lambda \ln\left(J^{\mathrm{el}}\right)\delta_{ij}\right] + \frac{1}{\varepsilon}\left(D_iD_j - \frac{1}{2}D_kD_k\delta_{ij}\right). \tag{41}$$

$$\mu^{s-\mathrm{electrolyte}} = RT\ln\frac{1}{1+\sum_{j\neq s}v^jC^j}. \tag{42}$$

$$\mu^{m-\mathrm{electrolyte}} = RT\left\{\ln\frac{v^mC^m}{1+\sum_{j\neq s}v^jC^j} + 1 - \frac{v^mC^m}{1+\sum_{j\neq s}v^jC^j}\right\} + FVz^m. \tag{43}$$

$$\mu^{m-\mathrm{OMIEC}} = RT\left\{\ln\frac{v^mC^m}{1+\sum_j v^jC^j} + \left(1-\frac{v^mC^m}{1+\sum_j v^jC^j}\right)\left(1+\frac{\chi^m}{1+\sum_j v^jC^j}\right)\right\} + FVz^m - \sigma^{\mathrm{m}}v^m \tag{44}$$

$$\mu^{\mathrm{h}} = RT\ln\frac{C^{\mathrm{h}}}{C^{\mathrm{h0}}} + FV. \tag{45}$$

$$\begin{aligned}\mu^{\phi} &= \mu^{I,0} - \mu^{II,0} + RT\left[\frac{\ln\phi+1}{N^I} - \frac{\ln(1-\phi)+1}{N^{II}} + \chi^{\phi}(1-2\phi)\right] \\ &+ \frac{RTa^2}{36}\frac{(1-2\phi)}{\phi^2(1-\phi)^2}(\nabla\phi)^2 - \frac{4\Delta\gamma}{\rho^{\mathrm{sub}}d\left(1+\frac{X_2}{d}\right)^3} - RTa^2\left(\frac{\chi^{\phi}}{3} + \frac{1}{18\phi(1-\phi)}\right)\nabla^2\phi.\end{aligned} \tag{46}$$

Eqs. (26) and (40) result in the following correspondence between the electrical displacement and the electrical field,

$$E_i = H_{iJ}\widetilde{E}_J = H_{iJ}\frac{\partial W}{\partial \widetilde{D}_J} = H_{iJ}\frac{\partial}{\partial \widetilde{D}_J}\left(\frac{1}{2\varepsilon}\frac{C_{KL}}{\det\boldsymbol{F}}\widetilde{D}_K\widetilde{D}_L\right) = H_{iJ}\left(\frac{1}{\varepsilon}\frac{F_{sJ}F_{sL}}{\det\boldsymbol{F}}\widetilde{D}_L\right) = \frac{1}{\varepsilon}D_i, \tag{47a}$$

or

$$D_i = \varepsilon E_i, \tag{47b}$$

where $F_{sJ}H_{iJ} = \delta_{si}$.

Under thermodynamic equilibrium, the chemical potential of the solvent in the electrolyte is the same as that in the OMIEC, namely

$$\mu^{s-\mathrm{electrolyte}} = \mu^{s-\mathrm{OMIEC}}. \tag{48}$$

Using Eqs. (42) and (44), we can define the osmotic pressure of the solvent as follows,

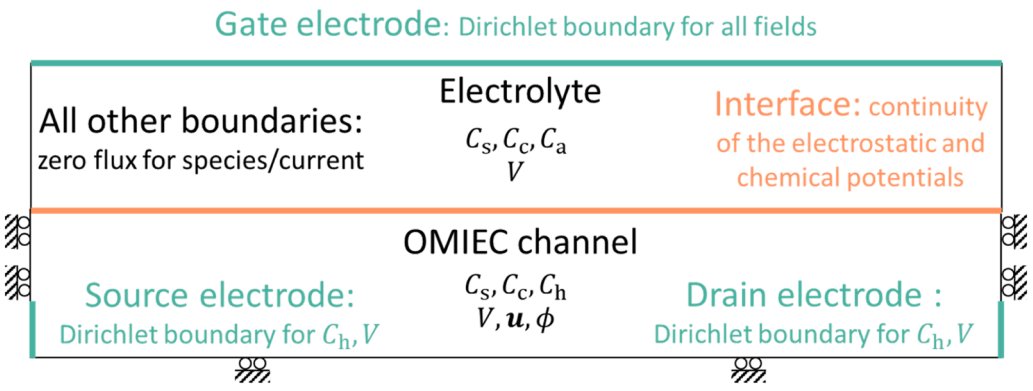

Fig. 3. Sketch of the OECT model with the geometry, field variables, and boundary conditions.

$$\sigma^{\mathrm{m}} = \frac{RT}{v^s}\left[\ln\frac{v^s C^s}{1+\sum_j v^j C^j} + \left(1-\frac{v^s C^s}{1+\sum_j v^j C^j}\right)\left(1+\frac{\chi^s}{1+\sum_j v^j C^j}\right) - \ln\frac{1}{1+\sum_{j\neq s} v^j C^j}\right] \tag{49}$$

Note that the last term is evaluated in the electrolyte and others are evaluated in the OMIEC.

3. A model of organic electrochemical transistors

3.1. Geometry, variable domains, and boundary conditions

We implement the theory into a finite element model and study the mechanics and electrochemistry of an OECT. The OECT is represented by a two-domain model as shown in Fig. 3. The gate electrode is on the top of the electrolyte, and the source and drain electrodes are at two sides of the channel in the lower domain. The electrolyte domain contains the variables of the concentrations of solvent C_{s}, cations C_{c}, anions C_{a}, and the electrostatic potential V, which are solved using the transport kinetics for the mobile species (Eqs. (10), (25), (29), (42), (43)) and the electrostatics (Eqs. (12), (13), (26), (47)). For simplicity, we assume that anions are restrained in the electrolyte and cations are the messenger between the electrolyte and the OMIEC. The OMIEC in the channel domain hosts variables of the concentrations of solvent C_{s}, cations C_{c}, holes C_{h}, the electrical potential V, the displacement $\boldsymbol{u}$, and the phase parameter ϕ, which are solved using the transport kinetics for the mobile species (Eqs. (10), (26), (29), (42), (44), (45)), evolution of the phase parameter (Eqs. (11), (28), (29), (46)), electrostatics (Eqs. (12), (13), (26), (47)), and the mechanics equations (Eqs. (5), (6), (9), (18), (21), (41)). A detailed description of the initial-boundary value problem is shown in Appendix C. To avoid the accumulation of holes in the PSS-rich region due to the accumulation of negative charges and ensure that the holes only appear in the PEDOT phase and cations in the PSS phase (Rebetez et al., 2022), the space charge concentration in Eq. (12) is modified as follows

$$Q = \left(\phi C_{\mathrm{h}} + (1-\phi)C_{\mathrm{c}} - (1-\phi)C_{\mathrm{fix}}\right)F, \tag{50}$$

where C_{fix} is the concentration of fixed negative charges in the pure PSS. Therefore, in the PSS-rich region with small ϕ, the contribution from cations $(1-\phi)C_{\mathrm{c}}$ to the space charge dominates and the contribution from the holes ϕC_{h} is negligible.

The initial and boundary conditions of the model are prescribed as follows. To avoid singularity in the electrochemical potential of species, the initial value of the solvent, cations, and holes in the OMIEC is set as a small value, as listed in Table 1. The OMIEC domain is roller-constrained (with freedom of motion in the vertical direction due to the swelling of OMIEC but not in the horizontal direction) in all the boundaries except that in contact with the electrolyte, and the rigid motion is suppressed. The top surface is assigned as the gate electrode with $C_{\mathrm{s}} = C_{\mathrm{s0}}$, $C_{\mathrm{c}} = C_{\mathrm{c0}}$, $C_{\mathrm{a}} = C_{\mathrm{a0}}$, and $V = V_G$. The source electrode on the lower left corner is with $C_{\mathrm{h}} = C_{\mathrm{h0}}$ and $V = 0$, and the drain electrode on the lower right corner is with $C_{\mathrm{h}} = C_{\mathrm{hD}}$ and $V = V_{\mathrm{D}}$. The electrostatic potential V and the electrochemical potentials of solvents and cations are continuous across the interface between the OMIEC and the electrolyte. The parameters used in the initial and boundary conditions are listed in Table 1.

The parameters for the free energy due to mechanical deformation are listed in Table 2. To improve the convergence, we adopted a linear hardening law with a tangent modulus of 2% of the shear modulus. The parameters for the free energy of mobile species and the electrical field are listed in Table 3. The diffusivities are listed in Table 4. We assume that the PEDOT phase conducts only holes and the PSS phase conducts only ions. This is realized by a phase parameter-dependent diffusivity, as shown in Table 4. We use the experimental measurements of an OECT from Tang et al. (Tang et al., 2021) as the benchmark. The size of the channel is as follows due to the computational cost: length $l = 120$nm, thickness $h = 60$nm, and width (out-of-plane direction) $w = 20$mm.

Table 1
Parameters for the initial and boundary conditions.

Parameter	Description	Value	Refs.
C_{sinit}	Initial value of solvent in OMIEC	1 mol m^{-3}	—
C_{cinit}	Initial value of cation in OMIEC	1 mol m^{-3}	—
C_{s0}	Concentration of solvent at the gate electrode	$1/v_{\mathrm{s}}$	Table 3
C_{c0}	Concentration of cations and anions at the gate electrode	200 mol m^{-3}	—
C_{fix}	Concentration of fixed charges in OMIEC	4000 mol m^{-3}	Szymański et al., 2017; Tybrandt et al., 2017; Volkov et al., 2017; Kaphle et al., 2020
C_{h0}	Concentration of holes at the source electrode	4000 mol m^{-3}	Szymański et al., 2017; Tybrandt et al., 2017; Volkov et al., 2017; Kaphle et al., 2020
C_{hinit}	Initial condition for concentration of holes	1 mol m^{-3}	—
C_{hD}	Concentration of holes at the drain electrode	$C_{\mathrm{h0}}\exp\left(\frac{F(V_S - V_D)}{RT}\right)$molm^{-3}	—

Table 2
Parameters for the free energy due to mechanical deformation.

Parameter	Description	Value	Refs.
G	Shear modulus	230 MPa	Lang et al., 2009
ν	Poisson's ratio	0.32	
λ	Lamé constant	409 MPa	
Y	Yield strength	17 MPa	

Table 3
Parameters for the free energy of mobile species and the electrical field.

Parameter	Description	Value	Refs.
N_1, N_2	Number of monomers per PEDOT/PSS chain	70, 2300	Xia and Ouyang, 2012
χ^{ϕ}	Flory parameter of mixing	0.5	Gennes, 1979
a	Characteristic chain length	$0.442\ \sqrt{N_1\phi + N_2(1-\phi)}$ nm	Gennes, 1979
$\Delta\gamma$	Difference of surface energy between PEDOT-substrate and PSS-substrate	5 mN m^{-1}	Saito et al., 2020
ρ^{sub}	Molar density of substrate	$\frac{2.2\ \text{g cm}^{-3}}{60\ \text{g mol}^{-1}}$	SiO_2
d	Interaction length	0.353 nm	Palumbiny et al., 2015
ε	Dielectric constant	81	Volkov et al., 2017
v^s, v^c	Molar volume of solvent and cation	$\frac{18\ \text{g mol}^{-1}}{0.997\ \text{g cm}^{-3}}$	Water
v^a	Molar volume of anion	$\frac{287.075\ \text{g mol}^{-1}}{1.33\ \text{g cm}^{-3}}$	$TFSI^-$
χ^m	Flory parameter of mixing for hydration	0.17	Bießmann et al., 2018

Table 4
Diffusivities.

Parameter	Types of species	Value	Refs.
D_{ϕ}	OMIEC chains	5×10^{-17} m^{2}s^{-1}	Richards and Jones, 1999
$D_{s-\text{electrolyte}}$	Solvent in electrolyte	10^{-8} m^{2}s^{-1}	Tybrandt et al., 2017
$D_{s-\text{OMIEC}}$	Solvent in OMIEC	10^{-14} m^{2}s^{-1}	Tybrandt et al., 2017
$D_{m-\text{electrolyte}}$	Ions in electrolyte	10^{-8} m^{2}s^{-1}	Tybrandt et al., 2017
$D_{c-\text{OMIEC}}$	Cations in OMIEC	$(10^{-14}\phi + 10^{-8}(1-\phi))$ m^{2}s^{-1}	Tybrandt et al., 2017
D_{h}	Holes in OMIEC	$10^{-8}\exp\left(-\frac{(\phi-0.5)^2}{2\times0.1^2}\right)$ m^{2}s^{-1}	Tybrandt et al. 2017

3.2. Implementation of the finite element model

When the polymer chains of PEDOT: PSS diffuse, the holes in PEDOT and ions in PSS are also in motion. We idealize and describe this process using a source term in the diffusion equations of ions and holes in the OMIEC

$$\dot{r}^{\text{h}} = \dot{\phi}C^{\text{h}}, \tag{51a}$$

$$\dot{r}^{\text{C}} = -\dot{\phi}C^{\text{C}}. \tag{51b}$$

The weak form is obtained for the transport equations by multiplying the differential form with a test function $\widehat{C}^m$ and integrate over the volume,

$$\int_{\Omega}\left(\dot{C}^m - \dot{r}^m + \frac{\partial J_K^m}{\partial X_K}\right)\widehat{C}^m \mathrm{d}\Omega = \int_{\Omega}(\dot{C}^m - \dot{r}^m)\widehat{C}^m \mathrm{d}\Omega + \int_{\Omega}\frac{C^m D^m}{RT}C_{IJ}^{-1}\frac{\partial \mu^m}{\partial X_I}\frac{\partial \widehat{C}^m}{\partial X_J}\mathrm{d}\Omega + \int_{S}\widehat{C}^m J_K^m N_K \mathrm{d}S. \tag{52}$$

where m represents the solvent, cation, anion, hole, and phase parameter. We solve the weak form of all the transport equations by COMSOL Multiphysics. The electrostatic field, the displacement field, and the electromechanical coupling are solved by the embedded modules in COMSOL. Third-order shape function is employed for the displacement field, while second-order shape functions are used for all other fields. The built-in time-dependent solver MUMPS (MUltifrontal Massively Parallel sparse direct Solver) is used to solve

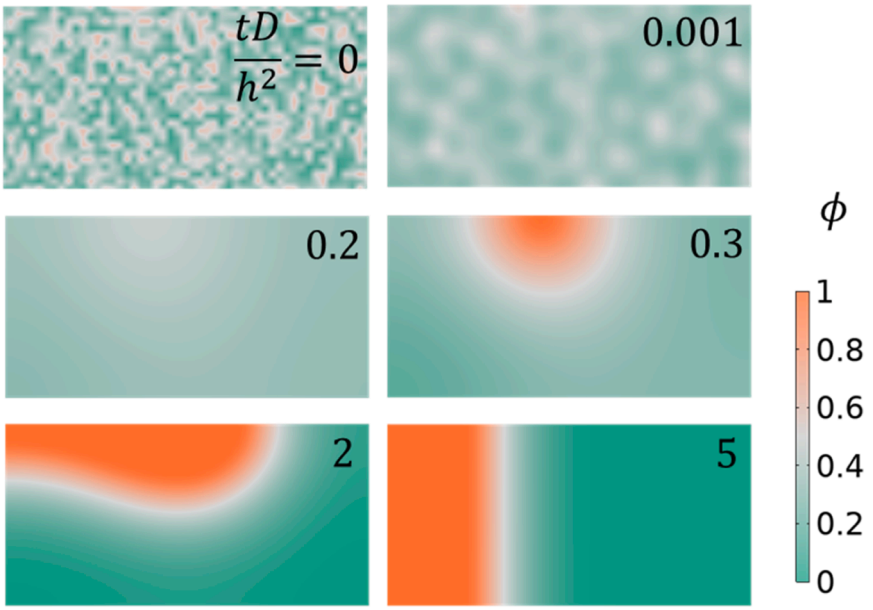

Fig. 4. Evolution of local volume fraction of PEDOT for $D_\phi = 5 \times 10^{-17}$ m^2/s at the normalized time $\frac{tD}{h^2} = 0$, 0.001, 0.2, 0.3, 2, and 5.

the equations of mechanical deformation and electrostatic field, and the weak formulation of the transport equations. The mesh convergence and algebraic convergence are satisfied.

4. Results

4.1. Phase behavior

Phase separation takes much longer time than the electrochemical doping of OMIECs. For PEDOT:PSS, electrochemical doping completes in less than 0.1 s (Kawahara et al., 2012). However, the time scale for the complete phase separation in PEDOT:PSS ranges from hours to days, depending on the experimental synthesis conditions and size of the samples. For a dimethyl sulfoxide-treated

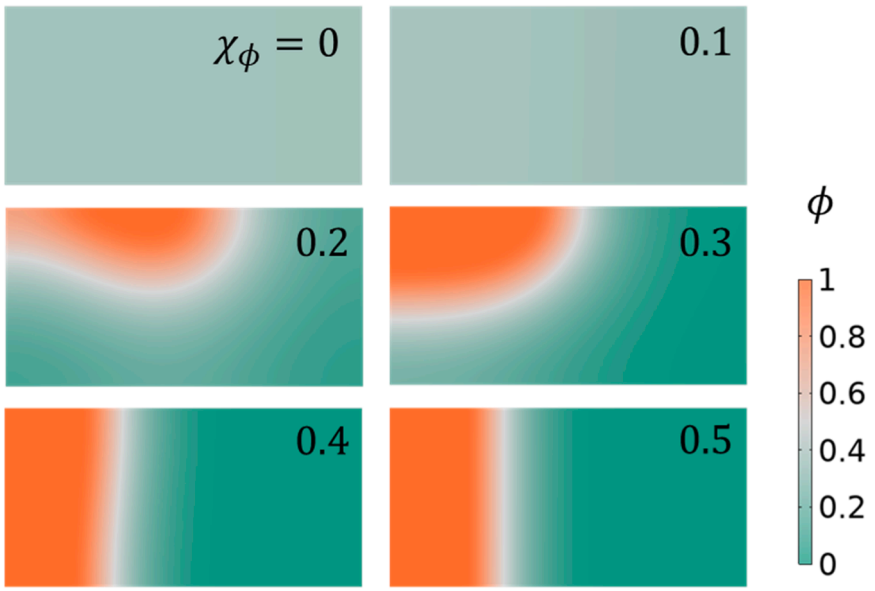

Fig. 5. Local volume fraction of PEDOT at the normalized time $\frac{tD}{h^2} = 5$ with the Flory parameter of mixing $\chi_\phi = 0 \sim 0.5$.

PEDOT:PSS thin-film of the size 4 cm × 2 cm × 1μm, in-plane phase separation is observed in 24 h, as shown in Fig. S1 (a–d). Vertical phase separation through the thickness direction requires a much smaller diffusion length. As indicated by the phase images in Fig. S1 (e–h), PSS aggregates at the top of the PEDOT:PSS films of the thickness ~ 90 nm within one hour. The difference in the time scale of the phase separation and the electrochemical doping implies that significant influence of phase separation occurs mostly after long-term cycling, but its impact on the local conduction path may be continuous throughout the cycling processes.

In this subsection, we study the phase behavior of two-phase OMIECs and explore the material parameters space, including the diffusivity, the Flory parameter of mixing, the molecular size of the PEDOT:PSS chains, and the interfacial energy between the OMIEC and the substrate, that govern the phase evolution. For simplicity, only the phase field is computed in this subsection while the electrochemistry and mechanics studies are presented in later sections. A random initial phase structure is generated to simulate the well-mixed phase structure after the solution processing (Li et al., 2019), as shown in Fig. 4 when $\frac{tD}{h^2} = 0$. We use the film thickness as the characteristic length of OMIEC diffusion in thin films. The average phase parameter ϕ is set 0.35, corresponding to the average volume fraction of PEDOT in the PEDOT:PSS mixture (Xia and Ouyang, 2012).

We first examine the phase evolution without the substrate effect, namely $w(X_2) = 0$. In this case, the system evolves to minimize the interfacial energy of the two-phase interfaces. Two stages can be roughly identified from the contour plots of the phase parameter, shown in the temporal order in Fig. 4. In the early stage (normalized time $\frac{tD}{h^2} < 0.2$), small-scale two-phase interfaces gradually disappear because of the high energy cost and relatively short diffusion length. In the later stage, large-scale phase separation emerges due to the excess energy of the interfaces in the mixed phase. The final equilibrium state exhibits horizontally separated phases with a small interfacial area. While a well-mixed phase structure enables balanced and fast charge conduction, a completely separated phase structure blocks the conduction of the charge carriers. Therefore, the evolution in Fig. 4 indicates that the overall conductivity peaks at $\frac{tD}{h^2} \sim 0.2$ when the phases are well mixed and then gradually declines to zero when the PSS and PEDOT phases are completely segregated from each other. We will validate this prediction in the next subsection.

The phase evolution is driven by the combined effects of the entropy of mixing and enthalpy of mixing. The Flory parameter for mixing χ_ϕ characterizes the enthalpy of mixing which strongly influences the shape of the free energy and the phase structure in equilibrium. For zero or small χ_ϕ, the entropy of mixing dominates in the free energy, which yields a coexisting phase, as shown in the case where $\chi_\phi = 0$ in Fig. 5. For large χ_ϕ, the enthalpy of mixing dominates, which favors phase separation as shown in $\chi_\phi \geq 0.2$ in Fig. 5. With larger χ_ϕ, phase separation is faster due to the higher driving force. Thus, the snapshots for $0.1 \leq \chi_\phi \leq 0.4$ obtained at $\frac{tD}{h^2} = 5$ also represent possible intermediate states toward the completely segregated state for $\chi_\phi = 0.5$. The results imply that, to optimize the electrochemical performance of well-mixed two-phase OMIECs, chemical additives in different treatment methods that result in low χ_ϕ are preferred to avoid large-scale phase separation.

The effect of entropy of mixing on the phase separation is also significant. Xia and Ouyang (2012) reported that PEDOT:PSS solutions with larger colloidal size exhibit higher conductivity. On the one hand, the colloidal size is influenced by the Flory parameter of mixing χ_ϕ, which is determined by the experimental synthesis conditions, additives, and so on. On the other hand, the colloidal size is

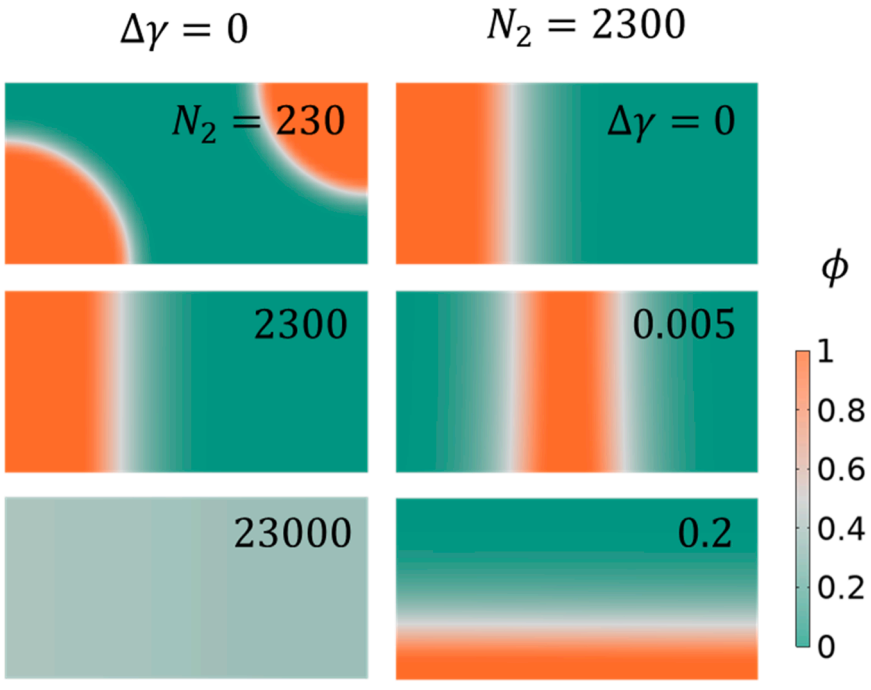

Fig. 6. Local volume fraction of PEDOT at the normalized time $\frac{tD}{h^2} = 5$ for $N_2 = 2300$ and $\Delta\gamma = 0$ N/m.

directly related to the molecular size, as proposed by Xia and Ouyang (2012). As shown in Eq. (33), the molecular size influences the entropy of mixing and the shape of the free energy which determines the phase structure and conductivity. Here, by increasing the number of monomers in the PSS chains we examine the phase behavior. As shown in the left panel of Fig. 6, large-scale phase separation occurs for $N_2 = 230$ and $N_2 = 2300$ at the normalized time $\frac{tD}{h^2} = 5$. However, the PSS chains with a larger molecular weight $N_2 = 23,000$ exhibit much slower phase separation and the phases coexist for a significantly longer time. When PEDOT and PSS coexist, the OMIEC is well doped with high conductivity. In contrast, large-scale phase separation destructs the conducting path and minimizes the conductivity. This explains the experimental observation on the colloidal size-dependent conductivity in PEDOT: PSS (Xia and Ouyang, 2012).

The presence of the substrate contributes to the free energy of mixing by $\phi w(X_2)$, according to Eq. (32). With this effect, the system evolves to minimize the interfacial energy of not only the two-phase interfaces but also the substrate-OMIEC interface. As shown in Fig. S1(e–h), PSS preferentially aggregates near the surface after solvent-vapor annealing (Yeo et al., 2012), which is in contrast with the in-plane phase separation as shown in Fig. S1(a–d) and discussed in Figs. 4 and 5. Here, we explore the substrate effect to uncover the mechanism. Assuming that the PEDOT-substrate interface has lower interfacial energy than the PSS-substrate interface, the substrate

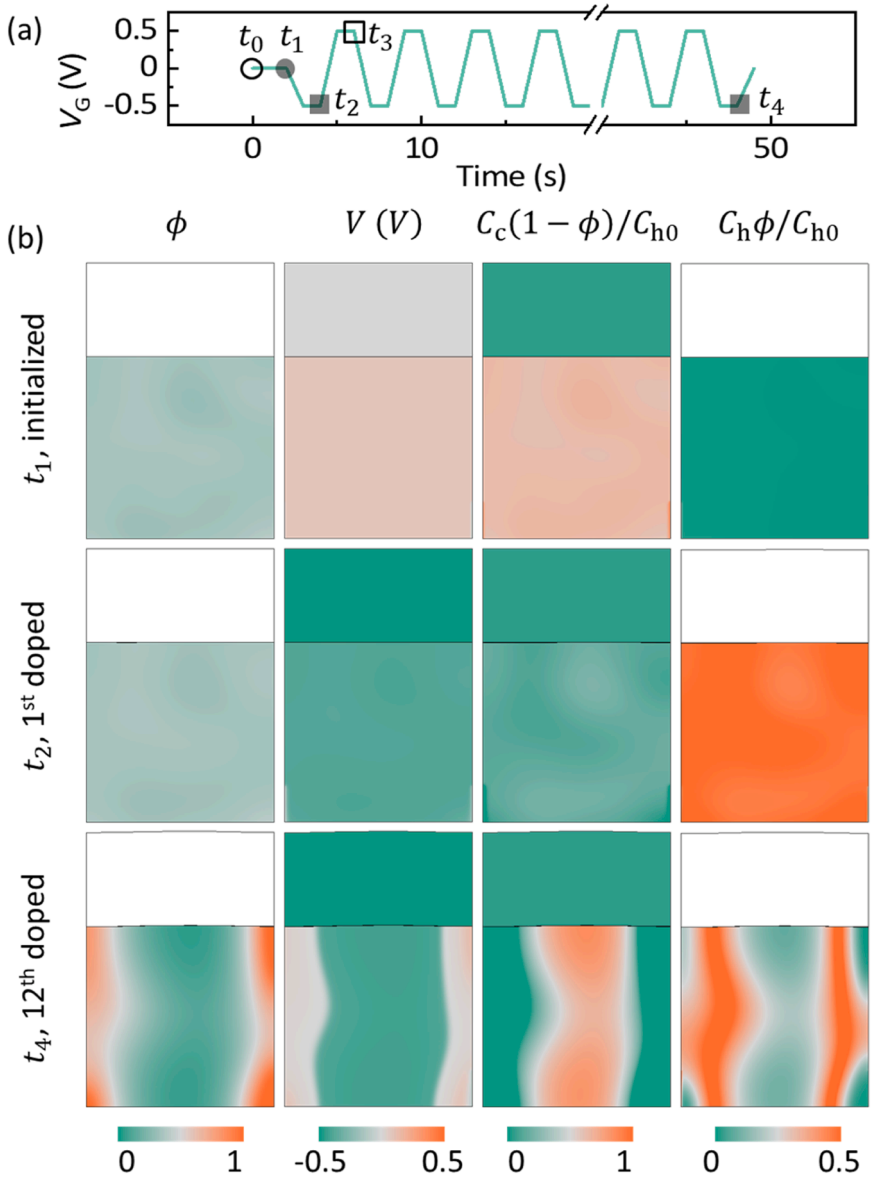

Fig. 7. (a) Gate voltage profile of the OECT during the 12 doping cycles. (b) Contours drawn in the deformed frame of the local volume fraction of PEDOT ϕ, the electrostatic potential V, the effective cation concentration $\frac{C_c(1-\phi)}{C_{h0}}$, and the effective hole concentration $\frac{C_h\phi}{C_{h0}}$ in the OECT at the initialized state t_1, the first doped state t_2, and the 12th doped state t_4.

would favor the presence of PEDOT, leading to vertical phase separation in the thickness direction. We choose the difference between the two interfacial energies $\Delta\gamma = \gamma_{\text{PSS-substrate}} - \gamma_{\text{PEDOT-substrate}}$ for the parametric study. For a given molecular weight of $N_2 = 2300$, we increase $\Delta\gamma$ from 0 to 0.2N/m. As mentioned above, when $\Delta\gamma = 0$, in-plane phase separation is more likely because of the smaller interfacial area in thin films. However, as shown in the right panel of Fig. 6 and when $\Delta\gamma = 0.2$N/m, higher $\Delta\gamma$ leads to vertical phase separation despite its larger two-phase interfacial area. Proper surface treatment can be used to obtain the desired phase structure and electrochemical performance.

4.2. Electrochemistry in an OECT

After examining the phase behavior in PEDOT: PSS, we now explore the electrochemistry of the two-phase OMIECs in an OECT device as the channel material. As described in the *Introduction*, OECTs control the current passing through the circuit via the applied gate and drain voltages. Specifically, the gate voltage controls the doping state of the channel and therefore its conductivity, and the drain voltage drives the current flow from the source electrode to the drain side.

In the following, we simulate the operation of an OECT and study the spatial and temporal distribution of the charge carriers in the OMIEC channel and the corresponding transfer curves of the OECT. The drain voltage is fixed at −0.1 V against the grounded source electrode, and the gate voltage is swept from −0.5 V to 0.5 V with a periodicity of four seconds, as shown in Fig. 7(a). As discussed in the previous subsection, doping of PEDOT: PSS takes less than one second, while the phase separation takes hours and even days to complete. To illustrate the influence of phase separation on the electrochemical performance of an OMIEC channel within several electrochemical doping cycles, the diffusivity of the polymer chains in the OMIEC is set to 5×10^{-17} m^2s^{-1} in the remaining text (Richards and Jones, 1999), which corresponds to a characteristic diffusion time of $\frac{h^2}{D} = 72$s in the thin film. Again, the film thickness has been used as the characteristic diffusion length since the channel in OECTs is typically several orders of magnitude longer than its thickness. All other parameters are listed in Tables 1–4.

We plot in Fig. 7(b) the contours of the local volume fraction of PEDOT ϕ, the electrostatic potential V, the effective cation concentration $\frac{C_c(1-\phi)}{C_{h0}}$, and the effective hole concentration $\frac{C_h\phi}{C_{h0}}$ at three selected states: t_1 – the initialized state, t_2 – the first doped state, and t_4 – the 12th doped state. As mentioned earlier and shown in Fig. 4, the initially generated phase structure features small-scale two-phase interfaces, which are highly unstable. At t_1, the average value of ϕ is 0.35 with a nearly uniform phase distribution. At t_4, large-scale heterogeneous phase structure emerges, where the PEDOT phase preferentially aggregates near the drain electrode.

The distribution of the charge carriers is determined by the electrical field and the phase structure. With a negative gate voltage, holes are injected from the source electrode to the PEDOT phase while cations are expelled from the PSS phase to the electrolyte, as shown in the doped state in Fig. 7(b). At a positive gate voltage, holes are removed from the OMIEC, and cations are recovered. The inhomogeneous phase structure influences the spatial distribution of the electrostatic potential and the concentration of the charge carriers in the OMIEC. This is shown in the contour plots of the 12th doped state. In the PSS-rich region (smaller ϕ), the presence of the fixed charges reduces the local voltage. And cations are transported to the PSS-rich region driven by the electrical field. In the meantime, the effective hole concentration is much higher at the two-phase interfaces than that in the PEDOT-rich domain because of the low hole conductivity in the crystallized PEDOT domains (Tybrandt et al., 2017; Shi et al., 2015). The excessive number of holes at the two-phase interface explains the origin of the so-called capacitive current in conjugated polymers (Volkov et al., 2017).

To reveal the effect of the phase evolution on the distribution of the field variables during the first 12 doping cycles, we select two points in the channel to demonstrate the different trends of the local volume fraction of PEDOT, as shown in Fig. 8(a). At point A, the volume fraction of PEDOT decreases. Therefore, the overall effective hole concentration $C_h\phi$ (dotted line) decreases over cycles, Fig. 8 (b). The overall effective cation concentration $C_c(1-\phi)$ (solid line) and the number of the fixed negative charge C^- (filled triangular symbols) increase because of the growth of the PSS phase. The space charge Q (empty square symbols), or the net charge at point A, remains vanishingly small for all the time. Therefore, the local electroneutrality is maintained, which agrees with the prediction by Wang et al. (2009). Meanwhile, the decreasing amplitude of both hole and cation indicates the diminishing electrochemical activity due to the phase segregation at this point. Likewise, the OMIEC domain at point B with an increasing amount of the PEDOT phase, in which case it becomes pure PEDOT at the end of the 12th cycle, also loses electrochemical activity. On the one hand, as the volume

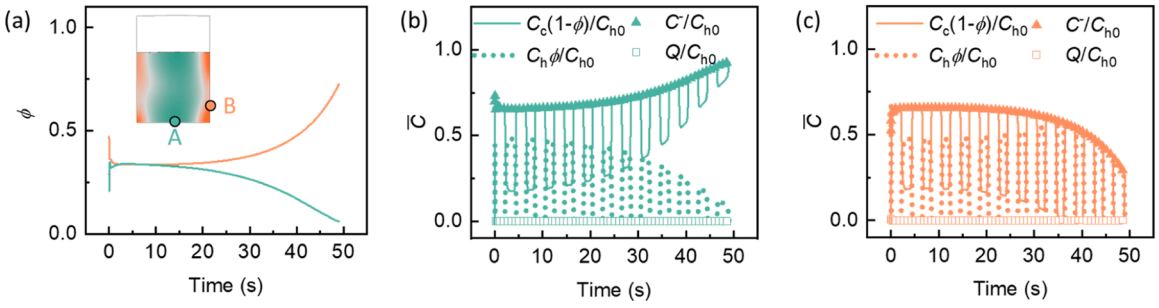

Fig. 8. Electrochemistry of OECT during the first 12 ON/OFF cycles. (a) The volume fraction of PEDOT at two locations A and B of the channel. The effective concentrations of cation $C_c(1-\phi)$ and hole $C_h\phi$, fixed negative charge C^-, and overall space charge Q at points A (b) and B (c).

fraction of PEDOT increases, the crystallinity in the PEDOT region may increase which retards the ionic diffusion and the electrochemical doping (Rebetez et al., 2022). This effect is represented in the diffusivities of cations and holes in Table 4. On the other hand, the decreasing amount of PSS leads to decreased number of negative charges to balance the positive charges in the PEDOT chains in the doped state. The slow diffusion and lack of charge-balancing species make doping of the PEDOT difficult. Therefore, the overall effective concentration of holes also decreases in this PEDOT-rich phase, as shown in Fig. 8(c). Note that we have neglected the diffusion of anions here which may additionally balance the positive charges in the PEDOT-rich domain. This effect should be rather small, because anion diffusion through the PSS-rich regions surrounding the PEDOT-rich region is significantly retarded due to the presence of negative fixed charges.

We now study the performance of an OECT by computing the drain current when sweeping the drain voltages and gate voltages. When the OECT is "ON" at a negative gate voltage, the output current is controlled by the drain voltage. The scaling law for the $I_D - V_D$ transfer curves in OECTs is expressed as follows (Rivnay et al., 2018),

$$I_{\mathrm{D}} \propto \mu^* C^* \frac{wh}{l} V_{\mathrm{D}}, \tag{53}$$

where μ^* is the carrier mobility, C^* is the capacitance, w is the width, h is the thickness, and l is the length of the channel.

In the experimental devices, the aspect ratios of the channel are significant with typical sizes of width w of millimeters, thickness h of tens of nanometers, and length l of tens of micrometers. Such high aspect ratios are hardly affordable in finite element modeling. To have a fair comparison between the experimental transfer curves and the modeling results, we apply a negative gate voltage -0.5 V and set the same values of μ^*, C^*, w, and h in the experiments, but use a much smaller value of l in the computational modeling. Following the scaling relation in Eq. (53) between I_D and l, we scale the drain current in the small-sized models ($l = 60$nm, 120nm) and present the results (solid line) against experimental data (dotted line, $l = 20\mu$m) in Fig. 9, in which the scaling factors 20μm /60nm and 20μm/120nm are used. The drain currents follow a monotonic relationship with respect to the drain voltage, which is in line with the prediction of Eq. (53). A more negative drain voltage induces a larger current from the source electrode to the drain electrode. The computational results for the OMIEC channel of the length of 60 nm and 120 nm compare reasonably well with the experiments, despite using constant values of μ^* and C^* which are likely dependent on the doping state. It is also worth noting that the drain current in the longer channel ($l = 120$nm) is larger at a given drain voltage, which is violating the scaling relation. This is due to the different phase behaviors in the two models where the longer channel shows a less degree of phase segregation while the drain voltage is swept, therefore, it has a higher conductivity than the shorter channel.

One of the most prominent features of OECTs is their ability to modulate the output current at the drain electrode using a small input voltage at the gate. To switch the OECT between the "ON" and "OFF" states for current modulation, we apply an alternating gate voltage from -0.5 to 0.5 V and a fixed drain voltage $V_{\mathrm{D}} = -0.1$V. The drain currents are plotted with solid lines in Fig. 9(b) against the experimental data (dotted line). The model successfully captures the current modulation between the ON—OFF states of an OECT. At negative gate voltages, the OMIEC is doped and the OECT is at the "ON" state which outputs a large current. Nevertheless, the drain current is nearly saturated when the gate voltage is beyond -0.5 V. At positive gate voltages, the OMIEC is dedoped and the OECT is turned off with a vanishingly small current. The logarithmic plot of the magnitude of the drain current in the inset of Fig. 9(b) reveals a difference of about six orders of magnitude in the drain current from the "ON" to the "OFF" state of the OECT device.

4.3. Mechanics in an OECT

Mechanical swelling of OMIECs. Mechanical swelling of polymeric materials such as hydrogels is well studied, as discussed in the *Introduction* section. Here, we focus on the influence of the electrochemical cycle and the resulting phase structure on the swelling behavior of OMIECs.

When a dry polymer OMIEC is in contact with a liquid electrolyte, the solvent and salt diffuse into the OMIEC and the host swells under entropic forces. The swelling is complete when the electrochemical potential of the mobile species, including the solvent and

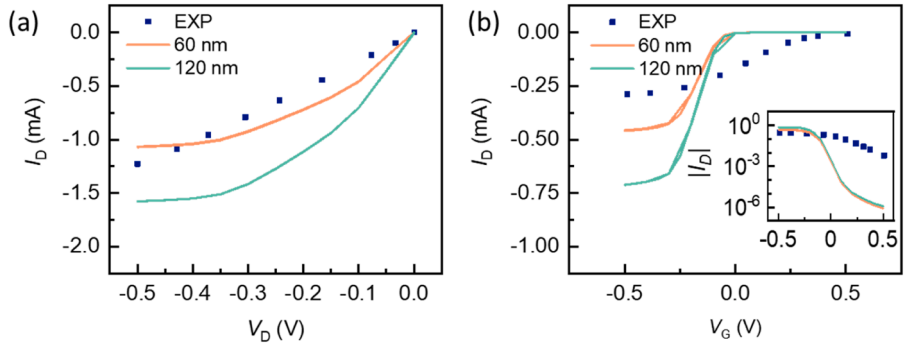

Fig. 9. (a) $I_{\mathrm{D}} - V_{\mathrm{D}}$ transfer curves at the doped state of the OMIEC, and (b) $I_{\mathrm{D}} - V_{\mathrm{G}}$ transfer curves of an OECT in the first doping and dedoping cycle of different channel lengths. Inset in (b) is the logarithmic scale of the absolute value of (b).

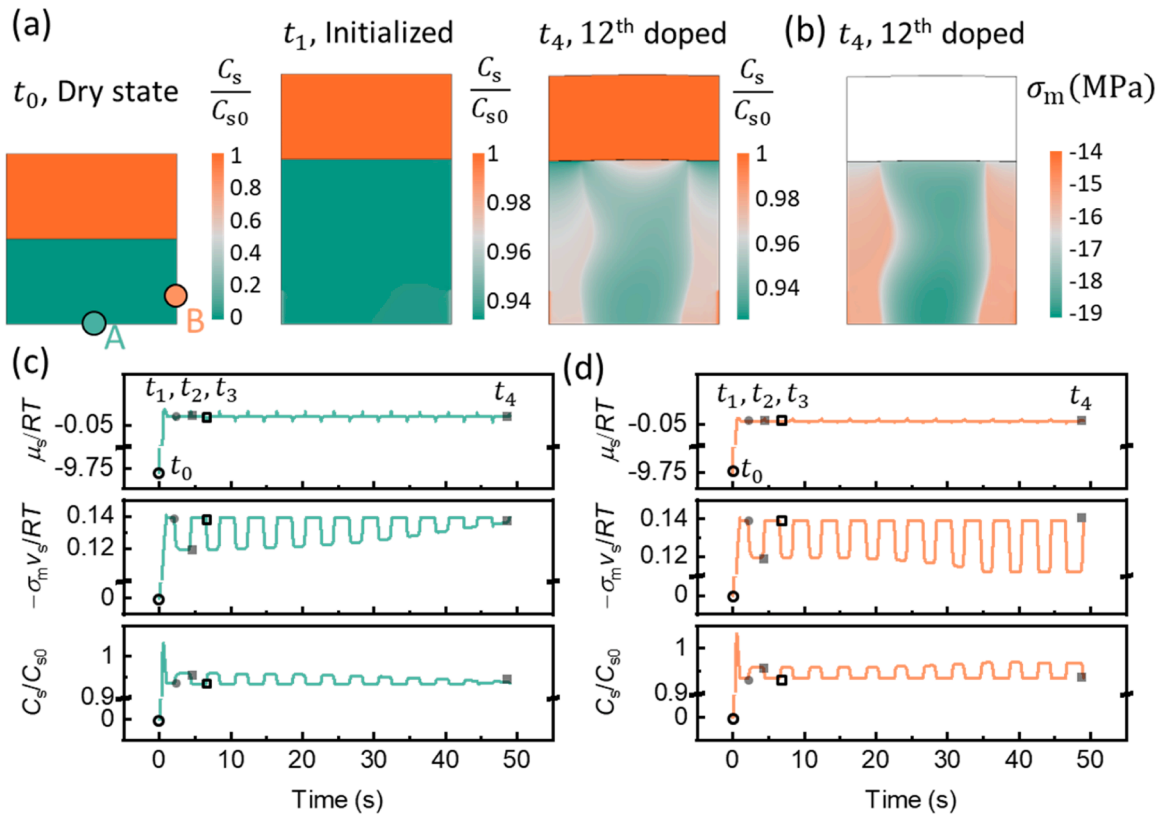

Fig. 10. Swelling of PEDOT:PSS in contact with electrolyte during the first 12 ON/OFF cycles. (a) The solvent concentration in the dry state, the first doped state, and the 12th doped state in the deformed configuration. (b) Mean stress distribution in the deformed configuration at the 12th doped state. Chemical potential, stress contribution to the chemical potential, and concentration of solvent in the PEDOT:PSS channel at point A (c) and point B (d).

cations, reaches equilibrium across the solid-liquid interface. Using the parameters listed in Table 3, the model predicts a volumetric strain of roughly 100% in PEDOT:PSS due to solvent absorption, as shown in Fig. 10(a). This agrees well with multiple experimental observations (Savva et al., 2018; Bießmann et al., 2018; Modarresi et al., 2020).

We plot the mean stress distribution in Fig. 10(b) at the 12th doped state. The inhomogeneous phase structure (Fig. 7(b)) causes non-uniform mean stresses across the channel because of the cation accumulation in the PSS-rich regions to balance the negative charges. We select points A and B again and show the temporal profile of the field quantities of the solvent in Fig. 10(c, d) to examine the influence of the electrochemical cycle on swelling. The chemical potential of the solvent in the electrolyte determined by Eq. (42) is close to zero for a dilute electrolyte. During the initialization process before t_1, the chemical potential of the solvent in the OMIEC reaches equilibrium and remains nearly a constant afterwards. At a negative gate voltage, the cations are expelled during the doping process (t_1 to t_2). This reduces the amount of swelling and the resultant compressive stress as shown in the middle panel of Fig. 10(c) and(d). The decreased stress contribution to the chemical potential of the solvent is then compensated by the increased entropic contribution via solvent absorption, as reflected in the jump in the solvent concentration from t_1 to t_2 in the bottom panel of Fig. 10(c) and (d). Upon dedoping, the entire process is reversed. When the cations are injected, the stress contribution to the chemical potential increases and the solvent concentration decreases from t_2 to t_3. Fig. S2 shows the swelling ratio of the PEDOT:PSS over the cycles. The change in solvent and cation concentrations alters the swelling ratio of the channel OMEIC from 1.94 at the doped state to 1.97 at the dedoped state, which is considerably smaller than the experimental measurement of poly(propylene dioxythiophene) (PProDOT) polymers in various electrolytes (Wang et al., 2020a, 2020b), which is about 20%~30%. The difference is likely due to the much larger size of the anions for charge-balancing in PProDOT films compared to the cation as the primary charge compensation carrier in PEDOT:PSS. In addition, the potentially substantial solvation shells of the counterions that are associated with additional swelling of the OMIEC are not accounted for in the current model.

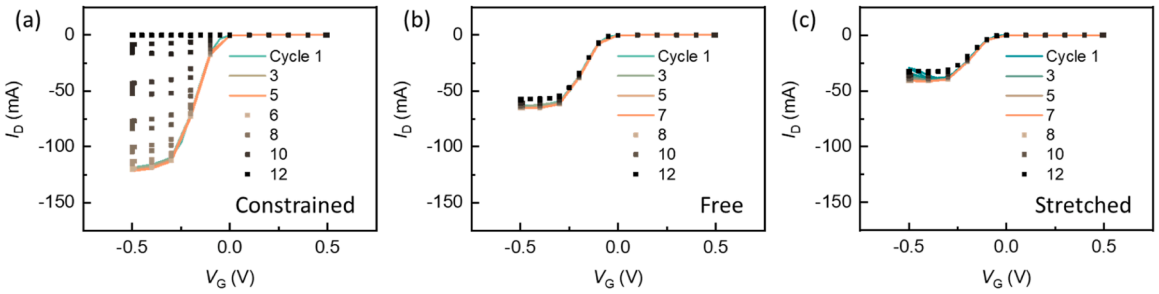

Fig. 11. Transfer curves of the OECT during 12 "ON—OFF" cycles at the (a) constrained state along the channel, (b) free expansion state, and (c) stretched state along the channel direction.

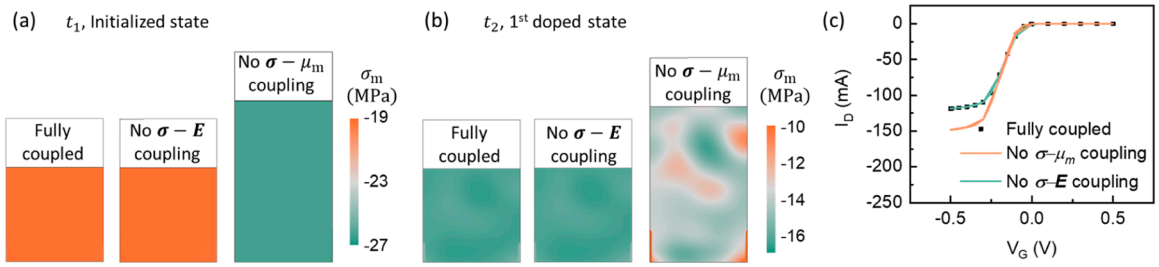

Fig. 12. Demonstration of the multiphysics coupling in an OECT device in the first ON/OFF cycle. Contour plots of the mean stress in the deformed channel at the initialized state (a) and the first doped state (b) of the channel. (c) Comparison between the transfer curves in the fully coupled model and without considering the electro-mechanical coupling or the stress-transport coupling.

We also study the swelling of OMIECs under stretched, free, and constrained states, since OECTs in bioelectronics are often subject to mechanical deformation such as due to the stretch of a skin sensor. The OMIEC is pre-deformed by 100% in the channel direction at the stretched state, and is fully constrained in the channel direction at the constrained state, while its vertical deformation toward the electrolyte is unconstrained in both cases. We plot the solvent concentration and deformation in Fig. S3. As the device changes from the stretched to the constrained state, the compressive stress increases, which, according to equation (42, 44), causes the decrease of the solvent concentration in the OMIEC at the swelled state. At the constrained state, the OMIEC swells to roughly 100% in the thickness direction. At the free state, the OMIEC swells up to 60% in both the thickness and channel directions. When it is stretched to two times its original length, the swelling in the thickness direction is about 40%. Overall, the aspect ratio of the OMIEC domain is changed from 1 at the constrained state to 3 at the stretched state.

OECT performance. In addition to the swelling of the OMIEC, mechanical stresses and the phase structure largely impact the OECT performance.

As discussed above, the material deformation due to an external load and swelling changes the aspect ratio of the OMIEC domain, which in turn modulates the phase evolution and eventually the OECT performance. We plot the transfer curves of OECTs at the stretched, free, and constrained states during 12 ON—OFF cycles in Fig. 11. The shape of the transfer curves is similar to those in Fig. 9 (b) but the peak current in the "ON" state changes. During the first few cycles, the phase parameter is almost uniform across the OMIEC domain, and the peak current remains about the same. After five cycles in the constrained model and seven cycles in the free and stretched models, the large-scale phase separation sets in, and the current starts to drop due to its influence on the conducting path. For the constrained OECT, in-plane phase separation occurs and the PEDOT phase accumulates near the source and drain electrodes which causes a high mobility of the phase parameter in the horizontal direction as shown in Fig. S3. As a result, PSS-rich regions emerge in the middle of the channel and hinder the electronic conduction from the source to the drain electrode. Therefore, the drain current diminishes after the 12th cycle in Fig. 11(a) even at the negative gate voltage which would have turned the transistor on. For the free and stretched OECTs, the mobility of the OMICE is more homogeneous and the complete phase separation has yet to occur, as shown in Fig. S3. The longer channel length for free and stretched OECTs requires a longer time for the transport of carriers from the source to the drain electrode and therefore the peak drain current is smaller than that in the constrained OECT.

OMIECs present a vivid example of multiphysics coupling at the interface between mechanics and electrochemistry. However, the

extent and significance of the coupling terms need to be discussed in the context. For instance, we showed in an earlier experiment that external pressure largely influences the doping kinetics of PProDOT in solid-state electrochromic devices (Wang et al., 2022). In the following, we explore the significance of the electromechanical coupling and the stress-transport coupling in OECTs. According to Eq. (41), the electromechanical coupling $\boldsymbol{\sigma} - \boldsymbol{E}$ is manifested by the Maxwell stress. And the stress-transport coupling is represented by $\sigma_{\mathrm{m}} \nu_m$ in the chemical potential of the mobile species, as shown in Eq. (44). By eliminating the Maxwell stress and the $\sigma_{\mathrm{m}} \nu_m$ term in the chemical potential of the mobile species, we compare the mechanical and the electrochemical responses in Fig. 12. The compressive stresses in the OMIEC lift the chemical potential of the solvents and cations. Therefore, the solvent and cation concentrations in the OMIEC are lower with the stress-transport ($\boldsymbol{\sigma} - \mu_m$) coupling, as indicated by the swelling ratio in Fig. 12(a) and (b). At the initialized state, the mean compressive stress is highest for the model without $\boldsymbol{\sigma} - \mu_m$ coupling due to the high swelling ratio. At the first doped state when the cations are expelled to the electrolyte, the swelling ratio slightly decreases and elastic unloading occurs, which reduces the stress level as shown in Fig. 12(b). The model without considering the stress-transport coupling shows a relatively smaller mean compressive stress field due to the extensive elastic unloading primarily by the solvent concentration change in the channel. The inhomogeneous stress profile in Fig. 12(b) is correlated to its phase distribution. When the stress-transport coupling is turned off, the solvent transport is only driven by the entropy and enthalpy of mixing within the channel and its distribution is homogeneous. Therefore, the PSS-rich regions experience larger compressive stress due to the cation accumulation. As for the transfer curves of the OECT, the model without $\boldsymbol{\sigma} - \mu_m$ coupling shows a higher peak current at the ON state. Notably, the model without the Maxwell stress shows little difference in both the mechanical and electrochemical responses from the fully coupled model. Therefore, the Maxwell stress can be eliminated in future models without sacrificing the accuracy of the predicted mechanical and electrochemical performance of the OECT.

5. Conclusions

In this work, we formulate a continuum theory of organic mixed ionic-electronic conductors of phase separation following the framework considering the thermodynamics laws, mass conservation, and the electrostatic field. We implement the theory into a finite element model and study the mechanics and the electrochemistry of the OMIEC in an organic electrochemical transistor. The computational modeling successfully captures several experimental observations such as the phase separation, mechanical swelling, conductivity variation, and capacitive current in a representative two-phase OMIEC. The model also replicates the transfer curves of an organic electrochemical transistor and predicts the failure of the device upon large-scale phase separation. We show that the deformation of the OMIEC influences phase evolution and leads to different phase behaviors and electrochemical performances in constrained/free/stretched OECTs. We also evaluate the extent of the electromechanical coupling and the stress-transport interaction in an OECT and show that the Maxwell stress is negligible. This work provides a theoretical basis for understanding the mechanics and electrochemistry of the current state-of-the-art two-phase OMIECs.

CRediT authorship contribution statement

Xiaokang Wang: Conceptualization, Methodology, Software, Writing – review & editing. **Kejie Zhao:** Supervision, Conceptualization, Writing – review & editing.

Declaration of competing interest

The authors declare that they have no known competing financial interests or personal relationships that could have appeared to influence the work reported in this paper.

Data availability

Data will be made available on request.

Acknowledgments

K.Z. and X.W. at Purdue University acknowledge the support by the National Science Foundation through Grant CMMI-2210158. We thank Prof. Jianguo Mei and his group for fruitful discussions during this work.

Appendix A

In this Appendix we show the detailed derivation for Eq. (16). We will evaluate each of the variation terms in Eq. (15) and simplify the terms related to the four types of works. First, the terms related to mechanical work are evaluated. From Eqs. (6) and (9), one has

$$F^{\mathrm{el}}_{i\mathscr{B}} = F_{iK} F^{-\mathrm{pl}}_{K\beta} F^{-\mathrm{C}}_{\beta\mathscr{B}}, \tag{A1}$$

$$F^{-\mathrm{C}}_{\alpha\mathscr{A}} = \Lambda^{-\frac{1}{3}}\delta_{\alpha\mathscr{A}}. \tag{A2}$$

Using Eqs. (A1) and (A2), we have

$$\begin{aligned}
\int_\Omega \frac{\partial W}{\partial \varepsilon^{\mathrm{el}}_{\mathscr{A}\mathscr{B}}}\delta\varepsilon^{\mathrm{el}}_{\mathscr{A}\mathscr{B}}\mathrm{d}\Omega &= \frac{1}{2}\int_\Omega \frac{\partial W}{\partial \varepsilon^{\mathrm{el}}_{\mathscr{A}\mathscr{B}}}\delta C^{\mathrm{el}}_{\mathscr{A}\mathscr{B}}\mathrm{d}\Omega = \int_\Omega \frac{\partial \mathrm{W}}{\partial \varepsilon^{\mathrm{el}}_{\mathscr{A}\mathscr{B}}}F^{\mathrm{el}}_{i\mathscr{A}}\delta F^{\mathrm{el}}_{i\mathscr{B}}\mathrm{d}\Omega = \int_\Omega \frac{\partial W}{\partial \varepsilon^{\mathrm{el}}_{\mathscr{A}\mathscr{B}}}F^{\mathrm{el}}_{i\mathscr{A}}\delta\left(F_{iK}F^{-\mathrm{pl}}_{K\beta}F^{-\mathrm{C}}_{\beta\mathscr{B}}\right)\mathrm{d}\Omega \\
&= \int_\Omega \frac{\partial W}{\partial \varepsilon^{\mathrm{el}}_{\mathscr{A}\mathscr{B}}}F^{\mathrm{el}}_{i\mathscr{A}}F^{-\mathrm{pl}}_{K\beta}F^{-\mathrm{C}}_{\beta\mathscr{B}}\delta(F_{iK})\mathrm{d}\Omega + \int_\Omega \frac{\partial W}{\partial \varepsilon^{\mathrm{el}}_{\mathscr{A}\mathscr{B}}}F^{\mathrm{el}}_{i\mathscr{A}}F_{iK}F^{-\mathrm{C}}_{\beta\mathscr{B}}\delta\left(F^{-\mathrm{pl}}_{K\beta}\right)\mathrm{d}\Omega \\
&\quad + \int_\Omega \frac{\partial W}{\partial \varepsilon^{\mathrm{el}}_{\mathscr{A}\mathscr{B}}}F^{\mathrm{el}}_{i\mathscr{A}}F_{iK}F^{-\mathrm{pl}}_{K\beta}\delta\left(F^{-\mathrm{C}}_{\beta\mathscr{B}}\right)\mathrm{d}\Omega \\
&= \int_\Omega \frac{\partial W}{\partial \varepsilon^{\mathrm{el}}_{\mathscr{A}\mathscr{B}}}F^{\mathrm{el}}_{i\mathscr{A}}F^{-\mathrm{pl}}_{K\beta}F^{-\mathrm{C}}_{\beta\mathscr{B}}\delta\left(\frac{\partial x_i}{\partial X_K}\right)\mathrm{d}\Omega \\
&\quad + \int_\Omega \frac{\partial W}{\partial \varepsilon^{\mathrm{el}}_{\mathscr{A}\mathscr{B}}}F^{\mathrm{el}}_{i\mathscr{A}}F_{iK}F^{-\mathrm{C}}_{\beta\mathscr{B}}\delta\left(F^{-\mathrm{pl}}_{K\beta}\right)\mathrm{d}\Omega + \int_\Omega \frac{\partial W}{\partial \varepsilon^{\mathrm{el}}_{\mathscr{A}\mathscr{B}}}F^{\mathrm{el}}_{i\mathscr{A}}F_{iK}F^{-\mathrm{pl}}_{K\beta}\delta\left(\Lambda^{-\frac{1}{3}}\delta_{\beta\mathscr{B}}\right)\mathrm{d}\Omega \\
&= \int_\Omega \frac{\partial}{\partial X_K}\left(\frac{\partial W}{\partial \varepsilon^{\mathrm{el}}_{\mathscr{A}\mathscr{B}}}F^{\mathrm{el}}_{i\mathscr{A}}F^{-\mathrm{pl}}_{K\beta}F^{-\mathrm{C}}_{\beta\mathscr{B}}\delta x_i\right)\mathrm{d}\Omega - \int_\Omega \delta x_i\frac{\partial}{\partial X_K}\left(\frac{\partial W}{\partial \varepsilon^{\mathrm{el}}_{\mathscr{A}\mathscr{B}}}F^{\mathrm{el}}_{i\mathscr{A}}F^{-\mathrm{pl}}_{K\beta}F^{-\mathrm{C}}_{\beta\mathscr{B}}\right)\mathrm{d}\Omega \\
&\quad + \int_\Omega \frac{\partial W}{\partial \varepsilon^{\mathrm{el}}_{\mathscr{A}\mathscr{B}}}F^{\mathrm{el}}_{i\mathscr{A}}F_{iK}F^{-\mathrm{C}}_{\beta\mathscr{B}}\delta\left(F^{-\mathrm{pl}}_{K\beta}\right)\mathrm{d}\Omega \\
&\quad + \int_\Omega -\frac{1}{3}\frac{\partial W}{\partial \varepsilon^{\mathrm{el}}_{\mathscr{A}\mathscr{B}}}F^{\mathrm{el}}_{i\mathscr{A}}F^{\mathrm{el}}_{i\mathscr{C}}F^{\mathrm{C}}_{\mathscr{C}\alpha}F^{\mathrm{pl}}_{\alpha K}F^{-\mathrm{pl}}_{K\beta}\Lambda^{-\frac{4}{3}}\delta_{\beta\mathscr{B}}\left(\sum_m\left(\frac{\partial\Lambda}{\partial C^m}\delta C^m\right)\right)\mathrm{d}\Omega \\
&= \int_S N_K\left(\frac{\partial W}{\partial \varepsilon^{\mathrm{el}}_{\mathscr{A}\mathscr{B}}}F^{\mathrm{el}}_{i\mathscr{A}}F^{-\mathrm{pl}}_{K\beta}F^{-\mathrm{C}}_{\beta\mathscr{B}}\delta x_i\right)^- - N_K\left(\frac{\partial W}{\partial \varepsilon^{\mathrm{el}}_{\mathscr{A}\mathscr{B}}}F^{\mathrm{el}}_{i\mathscr{A}}F^{-\mathrm{pl}}_{K\beta}F^{-\mathrm{C}}_{\beta\mathscr{B}}\delta x_i\right)^+\mathrm{d}S \\
&\quad - \int_\Omega \delta x_i\frac{\partial}{\partial X_K}\left(\frac{\partial W}{\partial \varepsilon^{\mathrm{el}}_{\mathscr{A}\mathscr{B}}}F^{\mathrm{el}}_{i\mathscr{A}}F^{-\mathrm{pl}}_{K\beta}F^{-\mathrm{C}}_{\beta\mathscr{B}}\right)\mathrm{d}\Omega + \int_\Omega \frac{\partial W}{\partial \varepsilon^{\mathrm{el}}_{\mathscr{A}\mathscr{B}}}F^{\mathrm{el}}_{i\mathscr{A}}F_{iK}F^{-\mathrm{C}}_{\beta\mathscr{B}}\delta\left(F^{-\mathrm{pl}}_{K\beta}\right)\mathrm{d}\Omega \\
&\quad + \int_\Omega -\frac{1}{3}\frac{\partial W}{\partial \varepsilon^{\mathrm{el}}_{\mathscr{A}\mathscr{B}}}F^{\mathrm{el}}_{i\mathscr{A}}F^{\mathrm{el}}_{i\mathscr{B}}\left(\sum_m\left(\frac{1}{\Lambda}\frac{\partial\Lambda}{\partial C^m}\delta C^m\right)\right)\mathrm{d}\Omega.
\end{aligned} \tag{A3}$$

Using Eq. (10a),

$$\begin{aligned}
&\int_\Omega -\frac{1}{3}\frac{\partial W}{\partial \varepsilon^{\mathrm{el}}_{\mathscr{A}\mathscr{B}}}F^{\mathrm{el}}_{i\mathscr{A}}F^{\mathrm{el}}_{i\mathscr{B}}\left(\sum_m\left(\frac{1}{\Lambda}\frac{\partial\Lambda}{\partial C^m}\delta C^m\right)\right)d\Omega = \sum_m\int_\Omega -\frac{1}{3}\frac{\partial W}{\partial \varepsilon^{\mathrm{el}}_{\mathscr{A}\mathscr{B}}}F^{\mathrm{el}}_{i\mathscr{A}}F^{\mathrm{el}}_{i\mathscr{B}}\frac{1}{\Lambda}\frac{\partial\Lambda}{\partial C^m}\left(-\frac{\partial J^m_L\delta t}{\partial X_L}+\delta r^m\right)d\Omega \\
&= \sum_m\int_\Omega J^m_L\delta t\frac{\partial}{\partial X_L}\left(-\frac{1}{3}\frac{\partial W}{\partial \varepsilon^{\mathrm{el}}_{\mathscr{A}\mathscr{B}}}F^{\mathrm{el}}_{i\mathscr{A}}F^{\mathrm{el}}_{i\mathscr{B}}\frac{1}{\Lambda}\frac{\partial\Lambda}{\partial C^m}\right)d\Omega \\
&\quad -\sum_m\int_S\left[N_L\left(-\frac{1}{3}\frac{\partial W}{\partial \varepsilon^{\mathrm{el}}_{\mathscr{A}\mathscr{B}}}F^{\mathrm{el}}_{i\mathscr{A}}F^{\mathrm{el}}_{i\mathscr{B}}\frac{1}{\Lambda}\frac{\partial\Lambda}{\partial C^m}J^m_L\delta t\right)^- - N_L\left(-\frac{1}{3}\frac{\partial W}{\partial \varepsilon^{\mathrm{el}}_{\mathscr{A}\mathscr{B}}}F^{\mathrm{el}}_{i\mathscr{A}}F^{\mathrm{el}}_{i\mathscr{B}}\frac{1}{\Lambda}\frac{\partial\Lambda}{\partial C^m}J^m_L\delta t\right)^+\right]\mathrm{d}S \\
&\quad +\sum_m\int_\Omega -\frac{1}{3}\frac{\partial W}{\partial \varepsilon^{\mathrm{el}}_{\mathscr{A}\mathscr{B}}}F^{\mathrm{el}}_{i\mathscr{A}}F^{\mathrm{el}}_{i\mathscr{B}}\frac{1}{\Lambda}\frac{\partial\Lambda}{\partial C^m}\delta r^m d\Omega.
\end{aligned} \tag{A4}$$

Combining Eqs. (14), (A3), and (A4), the terms related to mechanical energy in Eq. (15) reads the following.

$$
\begin{aligned}
&\int_{\Omega}\frac{\partial W}{\partial \varepsilon^{\mathrm{el}}_{\mathscr{A}\mathscr{B}}}\delta\varepsilon^{\mathrm{el}}_{\mathscr{A}\mathscr{B}}\mathrm{d}\Omega-\int_{\Omega}B_i\delta x_i\mathrm{d}\Omega-\int_{S}T_i\delta x_i\mathrm{d}S=-\int_{\Omega}\delta x_i\left[\frac{\partial}{\partial X_K}\left(\frac{\partial W}{\partial \varepsilon^{\mathrm{el}}_{\mathscr{A}\mathscr{B}}}F^{\mathrm{el}}_{i\mathscr{A}}F^{-\mathrm{pl}}_{K\beta}F^{-\mathrm{C}}_{\beta\mathscr{B}}\right)+B_i\right]\mathrm{d}\Omega\\
&-\int_{S}\left[N_K\left(\frac{\partial W}{\partial \varepsilon^{\mathrm{el}}_{\mathscr{A}\mathscr{B}}}F^{\mathrm{el}}_{i\mathscr{A}}F^{-\mathrm{pl}}_{K\beta}F^{-\mathrm{C}}_{\beta\mathscr{B}}\delta x_i\right)^{+}-N_K\left(\frac{\partial W}{\partial \varepsilon^{\mathrm{el}}_{\mathscr{A}\mathscr{B}}}F^{\mathrm{el}}_{i\mathscr{A}}F^{-\mathrm{pl}}_{K\beta}F^{-\mathrm{C}}_{\beta\mathscr{B}}\delta x_i\right)^{-}+T_i\delta x_i\right]\mathrm{d}S\\
&+\int_{\Omega}\frac{\partial W}{\partial \varepsilon^{\mathrm{el}}_{\mathscr{A}\mathscr{B}}}F^{\mathrm{el}}_{i\mathscr{A}}F_{iK}F^{-\mathrm{C}}_{\beta\mathscr{B}}\delta\left(F^{-\mathrm{pl}}_{K\beta}\right)\mathrm{d}\Omega+\sum_m\int_{\Omega}J^m_L\delta t\frac{\partial}{\partial X_L}\left(-\frac{1}{3}\frac{\partial W}{\partial \varepsilon^{\mathrm{el}}_{\mathscr{A}\mathscr{B}}}F^{\mathrm{el}}_{i\mathscr{A}}F^{\mathrm{el}}_{i\mathscr{B}}\frac{1}{\Lambda}\frac{\partial\Lambda}{\partial C^m}\right)\mathrm{d}\Omega\\
&-\sum_m\int_{S}\left[N_L\left(-\frac{1}{3}\frac{\partial W}{\partial \varepsilon^{\mathrm{el}}_{\mathscr{A}\mathscr{B}}}F^{\mathrm{el}}_{i\mathscr{A}}F^{\mathrm{el}}_{i\mathscr{B}}\frac{1}{\Lambda}\frac{\partial\Lambda}{\partial C^m}J^m_L\delta t\right)^{-}-N_L\left(-\frac{1}{3}\frac{\partial W}{\partial \varepsilon^{\mathrm{el}}_{\mathscr{A}\mathscr{B}}}F^{\mathrm{el}}_{i\mathscr{A}}F^{\mathrm{el}}_{i\mathscr{B}}\frac{1}{\Lambda}\frac{\partial\Lambda}{\partial C^m}J^m_L\delta t\right)^{+}\right]\mathrm{d}S\\
&+\sum_m\int_{\Omega}-\frac{1}{3}\frac{\partial W}{\partial \varepsilon^{\mathrm{el}}_{\mathscr{A}\mathscr{B}}}F^{\mathrm{el}}_{i\mathscr{A}}F^{\mathrm{el}}_{i\mathscr{B}}\frac{1}{\Lambda}\frac{\partial\Lambda}{\partial C^m}\delta r^m\mathrm{d}\Omega.
\end{aligned}
\tag{A5}
$$

For the terms related to all mobile species,

$$
\begin{aligned}
\sum_m\int_{\Omega}\frac{\partial W}{\partial C^m}\delta C^m\mathrm{d}\Omega\;&=\;\sum_m\int_{\Omega}\frac{\partial W}{\partial C^m}\left(-\frac{\partial J^m_K\delta t}{\partial X_K}+\delta r^m\right)\mathrm{d}\Omega=\sum_m\int_{\Omega}\frac{\partial W}{\partial C^m}\delta r^m\mathrm{d}\Omega+\sum_m\int_{\Omega}J^m_K\delta t\frac{\partial}{\partial X_K}\left(\frac{\partial W}{\partial C^m}\right)\mathrm{d}\Omega\\
&-\sum_m\int_{S}\left[N_K\left(J^m_K\delta t\frac{\partial W}{\partial C^m}\right)^{-}-N_K\left(J^m_K\delta t\frac{\partial W}{\partial C^m}\right)^{+}\right]\mathrm{d}S.
\end{aligned}
\tag{A6}
$$

Combining Eqs. (14), (A6), and (10b), the terms related to the energies of all mobile species in Eq. (15) reads the following.

$$
\begin{aligned}
&\sum_m\int_{\Omega}\frac{\partial W}{\partial C^m}\delta C^m\mathrm{d}\Omega-\sum_m\int_{\Omega}\mu^m\delta r^m\mathrm{d}\Omega-\sum_m\int_{S}\mu^m j^m\delta t\mathrm{d}S\\
&=\sum_m\int_{\Omega}\frac{\partial W}{\partial C^m}-\mu^m\delta r^m\mathrm{d}\Omega+\sum_m\int_{\Omega}J^m_K\delta t\frac{\partial}{\partial X_K}\left(\frac{\partial W}{\partial C^m}\right)\mathrm{d}\Omega\\
&+\sum_m\int_{S}\left[N_K\left(J^m_K\delta t\right)^{+}\left(\frac{\partial W}{\partial C^m}-\mu^m\right)^{+}-N_K\left(J^m_K\delta t\right)^{-}\left(\frac{\partial W}{\partial C^m}-\mu^m\right)^{-}\right]\mathrm{d}S.
\end{aligned}
\tag{A7}
$$

For the terms related to the electrical field, one obtains the following using Eqs. (12) and (13),

$$
\begin{aligned}
&\int_{\Omega}FV\delta r^{\mathrm{h}}\mathrm{d}\Omega=\int_{\Omega}FV\delta\left(\frac{Q}{F}-\sum_m z^mC^m-z^0C^0\right)\mathrm{d}\Omega\\
&=\int_{\Omega}V\delta Q-FV\sum_m z^m\delta C^m\mathrm{d}\Omega=\int_{\Omega}V\frac{\partial\delta\widetilde{D}_K}{\partial X_K}-FV\sum_m z^m\left(-\frac{\partial J^m_K\delta t}{\partial X_K}+\delta r^m\right)\mathrm{d}\Omega\\
&=-\int_{\Omega}\delta\widetilde{D}_K\frac{\partial V}{\partial X_K}\mathrm{d}\Omega+\int_{S}(\delta\widetilde{D}_KV)^{-}N_K-(\delta\widetilde{D}_KV)^{+}N_K\mathrm{d}S-\int_{\Omega}FV\sum_m z^m\delta r^m\mathrm{d}\Omega-\sum_m\int_{\Omega}J^m_K\delta tFz^m\frac{\partial V}{\partial X_K}\mathrm{d}\Omega\\
&+\sum_m\int_{S}FN_K\left(J^m_K\delta tz^mV\right)^{-}-FN_K\left(J^m_K\delta tz^mV\right)^{+}\mathrm{d}S.
\end{aligned}
\tag{A8}
$$

Combining Eqs. (14), (A8) and (10b), the terms related to the energy of the electrostatic field in Eq. (15) reads the following.

$$
\begin{aligned}
&\int_{\Omega}\frac{\partial W}{\partial\widetilde{D}_K}\delta\widetilde{D}_K\mathrm{d}\Omega-\int_{\Omega}FV\delta r^{\mathrm{h}}\mathrm{d}\Omega-\int_{S}FVj^{\mathrm{h}}\delta t\mathrm{d}S\\
&=\int_{\Omega}\left(\frac{\partial W}{\partial\widetilde{D}_K}+\frac{\partial V}{\partial X_K}\right)\delta\widetilde{D}_K\mathrm{d}\Omega+\int_{S}(\delta\widetilde{D}_KV)^{+}N_K-(\delta\widetilde{D}_KV)^{-}N_K\mathrm{d}S+\int_{\Omega}FV\sum_m z^m\delta r^m\mathrm{d}\Omega+\sum_m\int_{\Omega}J^m_K\delta tFz^m\frac{\partial V}{\partial X_K}\mathrm{d}\Omega\\
&+\int_{S}\left[F\left(\sum_m J^m_Kz^m+J^{\mathrm{h}}_K\right)^{+}V^{+}N_K-F\left(\sum_m J^m_Kz^m+J^{\mathrm{h}}_K\right)^{-}V^{-}N_K\right]\delta t\mathrm{d}S.
\end{aligned}
\tag{A9}
$$

The variation of the energy for the two-phase interface is

$$
\begin{aligned}
&\int_{\Omega}\left[\frac{\partial W}{\partial \phi}\delta\phi+\frac{\partial W}{\partial(\nabla\phi)_K}\delta(\nabla\phi)_K\right]\mathrm{d}\Omega=\int_{\Omega}\left[\frac{\partial W}{\partial \phi}\delta\phi+\frac{\partial W}{\partial(\nabla\phi)_K}\nabla(\delta\phi)_K\right]\mathrm{d}\Omega\\
&=\int_{\Omega}\left(\frac{\partial W}{\partial \phi}-\frac{\partial}{\partial X_K}\frac{\partial W}{\partial(\nabla\phi)_K}\right)\delta\phi\mathrm{d}\Omega+\int_{S}\left[N_K\left(\frac{\partial W}{\partial\nabla\phi}\right)_K^{-}-N_K\left(\frac{\partial W}{\partial\nabla\phi}\right)_K^{+}\right]\delta\phi\mathrm{d}S\\
&=\int_{\Omega}\left(\frac{\partial W}{\partial \phi}-\frac{\partial}{\partial X_K}\frac{\partial W}{\partial(\nabla\phi)_K}\right)\left(-\frac{\partial J_K^{\phi}\delta t}{\partial X_K}+\delta r^{\phi}\right)\mathrm{d}\Omega+\int_{S}\left[N_K\left(\frac{\partial W}{\partial(\nabla\phi)_K}\right)^{-}-N_K\left(\frac{\partial W}{\partial(\nabla\phi)_K}\right)^{+}\right]\delta\phi\mathrm{d}S\\
&=\int_{\Omega}\left(\frac{\partial W}{\partial \phi}-\frac{\partial}{\partial X_K}\frac{\partial W}{\partial(\nabla\phi)_K}\right)\delta r^{\phi}\mathrm{d}\Omega+\int_{\Omega}J_L^{\phi}\delta t\cdot\frac{\partial}{\partial X_L}\left(\frac{\partial W}{\partial \phi}-\frac{\partial}{\partial X_K}\frac{\partial W}{\partial(\nabla\phi)_K}\right)\mathrm{d}\Omega\\
&-\int_{S}\left[\left(\frac{\partial W}{\partial \phi}-\frac{\partial}{\partial X_K}\frac{\partial W}{\partial(\nabla\phi)_K}\right)J_L^{\phi}\delta t\right]^{-}N_L-\left[\left(\frac{\partial W}{\partial \phi}-\frac{\partial}{\partial X_K}\frac{\partial W}{\partial(\nabla\phi)_K}\right)J_L^{\phi}\delta t\right]^{+}N_L\mathrm{d}S\\
&+\int_{S}\left[N_K\left(\frac{\partial W}{\partial(\nabla\phi)_K}\right)^{-}-N_K\left(\frac{\partial W}{\partial(\nabla\phi)_K}\right)^{+}\right]\delta\phi\mathrm{d}S.
\end{aligned}
\tag{A10}
$$

Combining Eqs. (14) and (A10), the terms related to the energy of the two-phase interface in Eq. (15) reads the following.

$$
\begin{aligned}
&\int_{\Omega}\left[\frac{\partial W}{\partial \phi}\delta\phi+\frac{\partial W}{\partial(\nabla\phi)_K}\delta(\nabla\phi)_K\right]\mathrm{d}\Omega-\int_{\Omega}\mu^{\phi}(\boldsymbol{X},t)\delta r^{\phi}\mathrm{d}\Omega-\int_{S}\mu^{\phi}(\boldsymbol{X},t)\delta j^{\phi}\mathrm{d}S\\
&=\int_{\Omega}\left(\frac{\partial W}{\partial \phi}-\frac{\partial}{\partial X_K}\frac{\partial W}{\partial(\nabla\phi)_K}-\mu^{\phi}\right)\delta r^{\phi}\mathrm{d}\Omega\\
&+\int_{\Omega}J_L^{\phi}\delta t\frac{\partial}{\partial X_L}\left(\frac{\partial W}{\partial \phi}-\frac{\partial}{\partial X_K}\frac{\partial W}{\partial(\nabla\phi)_K}\right)\mathrm{d}\Omega\\
&-\int_{S}\left[\left(\frac{\partial W}{\partial \phi}-\frac{\partial}{\partial X_K}\frac{\partial W}{\partial(\nabla\phi)_K}-\mu^{\phi}\right)J_L^{\phi}\delta t\right]^{-}N_L-\left[\left(\frac{\partial W}{\partial \phi}-\frac{\partial}{\partial X_K}\frac{\partial W}{\partial(\nabla\phi)_K}-\mu^{\phi}\right)J_L^{\phi}\delta t\right]^{+}N_L\mathrm{d}S\\
&+\int_{S}\left[N_K\left(\frac{\partial W}{\partial(\nabla\phi)_K}\right)^{-}-N_K\left(\frac{\partial W}{\partial(\nabla\phi)_K}\right)^{+}\right]\delta\phi\mathrm{d}S.
\end{aligned}
\tag{A11}
$$

Combining equations (A5, A7, A9, A11) and (15), we obtain equation (16).

Appendix B

In this Appendix, we derive the stress expression in Eq. (41) using Eqs. (17), (31), (40). First, we examine the contribution of elastic deformation to stress.

$$
\begin{aligned}
&\frac{1}{\det(\boldsymbol{F})}\frac{\partial W^{\mathrm{el}}}{\partial\varepsilon^{\mathrm{el}}_{\mathscr{A}\mathscr{B}}}F^{\mathrm{el}}_{i\mathscr{A}}F^{\mathrm{el}}_{j\mathscr{B}}=\frac{F^{\mathrm{el}}_{i\mathscr{A}}F^{\mathrm{el}}_{j\mathscr{B}}}{\det(\boldsymbol{F})}\frac{\partial}{\partial\varepsilon^{\mathrm{el}}_{\mathscr{A}\mathscr{B}}}\left\{\frac{1}{2}G\left[I_1\left(C^{\mathrm{el}}\right)-3-2\ln\left(J^{\mathrm{el}}\right)\right]+\frac{1}{2}\lambda\left[\ln\left(J^{\mathrm{el}}\right)\right]^2\right\}\\
&=\frac{F^{\mathrm{el}}_{i\mathscr{A}}F^{\mathrm{el}}_{j\mathscr{B}}}{\det(\boldsymbol{F})}\frac{\partial}{\partial C^{\mathrm{el}}_{\mathscr{A}\mathscr{B}}}\left\{G\left[I_1\left(C^{\mathrm{el}}\right)-3-2\ln\left(J^{\mathrm{el}}\right)\right]+\lambda\left[\ln\left(J^{\mathrm{el}}\right)\right]^2\right\}\\
&=\frac{F^{\mathrm{el}}_{i\mathscr{A}}F^{\mathrm{el}}_{j\mathscr{B}}}{\det(\boldsymbol{F})}\left\{G\left(\delta_{\mathscr{A}\mathscr{B}}-C^{-\mathrm{el}}_{\mathscr{A}\mathscr{B}}\right)+\lambda\ln\left(J^{\mathrm{el}}\right)C^{-\mathrm{el}}_{\mathscr{A}\mathscr{B}}\right\}=\frac{1}{\det(\boldsymbol{F})}\left[G\left(C^{\mathrm{el}}_{ij}-\delta_{ij}\right)+\lambda\ln\left(J^{\mathrm{el}}\right)\delta_{ij}\right]\\
&=\frac{1}{\det(\boldsymbol{F})}\left[2G\varepsilon^{\mathrm{el}}_{ij}+\lambda\ln\left(J^{\mathrm{el}}\right)\delta_{ij}\right].
\end{aligned}
$$

The Maxwell stress is evaluated in the following.

$$\frac{1}{\det}(\boldsymbol{F})\frac{\partial W^{\mathrm{E}}}{\partial \varepsilon^{\mathrm{el}}_{\mathscr{A}\mathscr{B}}}F^{\mathrm{el}}_{i\mathscr{A}}F^{\mathrm{el}}_{j\mathscr{B}} = \frac{F^{\mathrm{el}}_{i\mathscr{A}}F^{\mathrm{el}}_{j\mathscr{B}}}{\det(\boldsymbol{F})}\frac{\partial}{\partial \varepsilon^{\mathrm{el}}_{\mathscr{A}\mathscr{B}}}\left(\frac{1}{2\varepsilon}\frac{C_{KL}}{\det\boldsymbol{F}}\widetilde{D}_K\widetilde{D}_L\right) = \frac{F^{\mathrm{el}}_{i\mathscr{A}}F^{\mathrm{el}}_{j\mathscr{B}}}{\det(\boldsymbol{F})}\frac{\partial}{\partial C^{\mathrm{el}}_{\mathscr{A}\mathscr{B}}}\left(\frac{1}{\varepsilon}\frac{C_{KL}}{\det\boldsymbol{F}}\widetilde{D}_K\widetilde{D}_L\right)$$

$$= \frac{F^{\mathrm{el}}_{i\mathscr{A}}F^{\mathrm{el}}_{j\mathscr{B}}}{\det(\boldsymbol{F})}\frac{\partial}{\partial C^{\mathrm{el}}_{\mathscr{A}\mathscr{B}}}\left(\frac{1}{\varepsilon}\frac{F^{\mathrm{inel}}_{\gamma K}F^{\mathrm{inel}}_{\lambda L}C^{\mathrm{el}}_{\gamma\lambda}}{\det\boldsymbol{F}}\widetilde{D}_K\widetilde{D}_L\right)$$

$$= \frac{1}{\varepsilon}\frac{F^{\mathrm{el}}_{i\mathscr{A}}F^{\mathrm{el}}_{j\mathscr{B}}}{\det(\boldsymbol{F})}\left(\frac{F^{\mathrm{inel}}_{\mathscr{A}K}F^{\mathrm{inel}}_{\mathscr{B}L}\widetilde{D}_K\widetilde{D}_L}{\det\boldsymbol{F}} - \frac{1}{2}\frac{C_{KL}\widetilde{D}_K\widetilde{D}_L\det\boldsymbol{F}^{\mathrm{inel}}\det\boldsymbol{F}^{\mathrm{el}}C^{-\mathrm{el}}_{\mathscr{A}\mathscr{B}}}{(\det\boldsymbol{F})^2}\right)$$

$$= \frac{1}{\varepsilon}\left(\frac{F_{iK}F_{jL}\widetilde{D}_K\widetilde{D}_L}{(\det\boldsymbol{F})^2} - \frac{1}{2}\frac{F_{sK}F_{sL}\widetilde{D}_K\widetilde{D}_L}{(\det\boldsymbol{F})^2}\delta_{ij}\right) = \frac{1}{\varepsilon}\left(D_iD_j - \frac{1}{2}D_kD_k\delta_{ij}\right).$$

Therefore,

$$\sigma_{ij} = \frac{1}{\det(\boldsymbol{F})}\frac{\partial W^{\mathrm{el}}}{\partial \varepsilon^{\mathrm{el}}_{\mathscr{A}\mathscr{B}}}F^{\mathrm{el}}_{i\mathscr{A}}F^{\mathrm{el}}_{j\mathscr{B}} + \frac{1}{\det(\boldsymbol{F})}\frac{\partial W^{\mathrm{E}}}{\partial \varepsilon^{\mathrm{el}}_{\mathscr{A}\mathscr{B}}}F^{\mathrm{el}}_{i\mathscr{A}}F^{\mathrm{el}}_{j\mathscr{B}} = \frac{1}{\det(\boldsymbol{F})}\left[2G\varepsilon^{\mathrm{el}}_{ij} + \lambda\ln\left(J^{\mathrm{el}}\right)\delta_{ij}\right] + \frac{1}{\varepsilon}\left(D_iD_j - \frac{1}{2}D_kD_k\delta_{ij}\right)$$

Appendix C

In this Appendix, we summarize the governing equations of the theory for describing the mechanical response, mass/charge transport, and electrostatics in the OECT model, as well as the initial and boundary conditions in the numerical modeling. The system consists of the OMIEC (volume Ω_{OMIEC} enclosed by surface S_{OMIEC}) and a liquid electrolyte (volume Ω_{liquid} enclosed by surface S_{liquid}).

The mechanics equations solve the displacement field $\boldsymbol{X}$ via the linear momentum balance equation:

$$\frac{\partial P_{iK}}{\partial X_K} + B_i = 0, \text{ in } \Omega_{\mathrm{OMIEC}} \tag{C1a}$$

$$T_i + N_K(P_{iK})^+ - N_K(P_{iK})^- = 0, \text{ in } S_{\mathrm{OMIEC}} \tag{C1b}$$

where

$$\sigma_{ij} = \frac{1}{\det(\boldsymbol{F})}P_{iK}F_{jK} = \frac{1}{\det(\boldsymbol{F})}\left[2G\varepsilon^{\mathrm{el}}_{ij} + \lambda\ln\left(\det\left(\boldsymbol{F}^{\mathrm{el}}\right)\right)\delta_{ij}\right] + \frac{1}{\varepsilon}\left(D_iD_j - \frac{1}{2}D_kD_k\delta_{ij}\right), \tag{C2a}$$

$$F_{iK} = \frac{\partial x_i}{\partial X_K} = F^{\mathrm{el}}_{i\mathscr{A}}F^{\mathrm{C}}_{\mathscr{A}\alpha}F^{\mathrm{pl}}_{\alpha K}, \tag{C2b}$$

$$C_{KL} = F_{iK}F_{iL}, \tag{C2c}$$

$$F^{\mathrm{C}}_{\mathscr{A}\alpha} = \Lambda^{\frac{1}{3}}\delta_{\mathscr{A}\alpha} \tag{C2d}$$

$$\det\left(\boldsymbol{F}^{\mathrm{C}}\right) = \Lambda = 1 + \sum_m C^m v^m. \tag{C2e}$$

G represents the shear modulus, λ Lamé parameter, ε the dielectric constant, v^m the volume of the mobile species m. The summation in Eq. (C2e) is over all the mobile ions and solvent in the solid. The initial and boundary conditions for the displacement in the model are prescribed in Fig. 3.

The yield condition and the plastic flow rule are the following.

$$F^{\mathrm{y}} = \sqrt{\frac{3}{2}\Sigma^{\mathrm{d}}_{KL}\Sigma^{\mathrm{d}}_{KL}} - \sigma^{\mathrm{y}}, \tag{C3a}$$

$$F^{-\mathrm{pl}}_{K\beta}\dot{F}^{\mathrm{pl}}_{\beta L} = \mathscr{H}\frac{\partial F_{\mathrm{y}}}{\partial \Sigma_{KL}}, \tag{C3b}$$

$$\mathscr{H} \geq 0,\ F_{\mathrm{y}} \leq 0,\ \mathscr{H}F_{\mathrm{y}} = 0, \tag{C3c}$$

$$\Sigma_{KL} = P_{iL}F_{iK}. \tag{C3d}$$

The governing equations for transport of the mobile species solve the concentration field C^{s}, C^{c}, C^{a}, and C^{h}:

$$\dot{C}^{\mathrm{s}} + \frac{\partial J^{\mathrm{s}}_K(\boldsymbol{X},t)}{\partial X_K} = 0, \text{ in } \Omega_{\mathrm{OMIEC}} \cup \Omega_{\mathrm{liquid}}, \tag{C4a}$$

$$N_K\left[J_K^{\mathrm{s}}(\boldsymbol{X},t)\right]^{+}-N_K\left[J_K^{\mathrm{s}}(\boldsymbol{X},t)\right]^{-}=j^{\mathrm{s}}(\boldsymbol{X},t),\ \text{in } S_{\mathrm{OMIEC}}\cup S_{\mathrm{liquid}}, \tag{C4b}$$

$$\mu^{\mathrm{s}}=RT\ln\frac{1}{1+\sum_{j\neq s}\nu^j C^j},\ \text{in } \Omega_{\mathrm{liquid}}, \tag{C4c}$$

$$\mu^{\mathrm{s}}=RT\left\{\ln\frac{\nu^{\mathrm{s}}C^{\mathrm{s}}}{1+\sum_j\nu^j C^j}+\left(1-\frac{\nu^{\mathrm{s}}C^{\mathrm{s}}}{1+\sum_j\nu^j C^j}\right)\left(1+\frac{\chi^{\mathrm{s}}}{1+\sum_j\nu^j C^j}\right)\right\}-\sigma^{\mathrm{m}}\nu^m\ \text{in } \Omega_{\mathrm{OMIEC}}, \tag{C4d}$$

$$J_K^{\mathrm{s}}=-\frac{C^{\mathrm{s}}D^{\mathrm{s}}}{RT}C_{KL}^{-1}\frac{\partial\mu^{\mathrm{s}}}{\partial X_L},\ \text{in } \Omega_{\mathrm{OMIEC}}\cup\Omega_{\mathrm{liquid}}, \tag{C4e}$$

$$\dot{C}^{\mathrm{c}}+\frac{\partial J_K^{\mathrm{c}}(\boldsymbol{X},t)}{\partial X_K}=0,\ \text{in } \Omega_{\mathrm{OMIEC}}\cup\Omega_{\mathrm{liquid}}, \tag{C5a}$$

$$N_K\left[J_K^{\mathrm{c}}(\boldsymbol{X},t)\right]^{+}-N_K\left[J_K^{\mathrm{c}}(\boldsymbol{X},t)\right]^{-}=j^{\mathrm{c}}(\boldsymbol{X},t),\ \text{in } S_{\mathrm{OMIEC}}\cup S_{\mathrm{liquid}}, \tag{C5b}$$

$$\mu^{\mathrm{c}}=RT\left\{\ln\frac{\nu^{\mathrm{c}}C^{\mathrm{c}}}{1+\sum_{j\neq s}\nu^j C^j}+1-\frac{\nu^{\mathrm{c}}C^{\mathrm{c}}}{1+\sum_{j\neq s}\nu^j C^j}\right\}+FVz^{\mathrm{c}},\ \text{in } \Omega_{\mathrm{liquid}}, \tag{C5c}$$

$$\mu^{\mathrm{c}}=RT\left\{\ln\frac{\nu^{\mathrm{c}}C^{\mathrm{c}}}{1+\sum_{j}\nu^j C^j}+1-\frac{\nu^{\mathrm{c}}C^{\mathrm{c}}}{1+\sum_{j}\nu^j C^j}\right\}+FVz^{\mathrm{c}}-\sigma^{\mathrm{m}}\nu^{\mathrm{c}},\ \text{in } \Omega_{\mathrm{OMIEC}}, \tag{C5d}$$

$$J_K^{\mathrm{c}}=-\frac{C^{\mathrm{c}}D^{\mathrm{c}}}{RT}C_{KL}^{-1}\frac{\partial\mu^{\mathrm{c}}}{\partial X_L},\ \text{in } \Omega_{\mathrm{OMIEC}}\cup\Omega_{\mathrm{liquid}}, \tag{C5e}$$

$$\dot{C}^{\mathrm{a}}+\frac{\partial J_K^{\mathrm{a}}(\boldsymbol{X},t)}{\partial X_K}=0,\ \text{in } \Omega_{\mathrm{liquid}}, \tag{C6a}$$

$$N_K\left[J_K^{\mathrm{a}}(\boldsymbol{X},t)\right]^{+}-N_K\left[J_K^{\mathrm{a}}(\boldsymbol{X},t)\right]^{-}=j^{\mathrm{a}}(\boldsymbol{X},t),\ \text{in } S_{\mathrm{liquid}}, \tag{C6b}$$

$$J_K^{\mathrm{a}}=-\frac{C^{\mathrm{a}}D^{\mathrm{a}}}{RT}C_{KL}^{-1}\frac{\partial\mu^{\mathrm{a}}}{\partial X_L},\ \text{in } \Omega_{\mathrm{liquid}}, \tag{C6c}$$

$$\mu^{\mathrm{a}}=RT\left\{\ln\frac{\nu^{\mathrm{a}}C^{\mathrm{a}}}{1+\sum_{j\neq s}\nu^j C^j}+1-\frac{\nu^{\mathrm{a}}C^{\mathrm{a}}}{1+\sum_{j\neq s}\nu^j C^j}\right\}+FVz^{\mathrm{a}},\ \text{in } \Omega_{\mathrm{liquid}}, \tag{C6d}$$

$$\dot{C}^{\mathrm{h}}+\frac{\partial J_K^{\mathrm{h}}(\boldsymbol{X},t)}{\partial X_K}=0,\ \text{in } \Omega_{\mathrm{OMIEC}}, \tag{C7a}$$

$$N_K\left[J_K^{\mathrm{h}}(\boldsymbol{X},t)\right]^{+}-N_K\left[J_K^{\mathrm{h}}(\boldsymbol{X},t)\right]^{-}=j^{\mathrm{h}}(\boldsymbol{X},t),\ \text{in } S_{\mathrm{OMIEC}}, \tag{C7b}$$

$$\mu^{\mathrm{h}}=RT\ln\frac{C^{\mathrm{h}}}{C^{\mathrm{h0}}}+FV,\ \text{in } \Omega_{\mathrm{OMIEC}}, \tag{C7c}$$

$$J_K^{\mathrm{h}}=-\frac{C^{\mathrm{h}}D^{\mathrm{h}}}{RT}C_{KL}^{-1}\frac{\partial\mu^{\mathrm{h}}}{\partial X_L},\ \text{in } \Omega_{\mathrm{OMIEC}}, \tag{C7d}$$

Specifically, we prescribed the following boundary and initial conditions in the model as shown in Fig. 3.

$$C^{\mathrm{s}}=\frac{1}{\nu^{\mathrm{s}}},\ C^{\mathrm{c}}=\frac{1}{\nu^{\mathrm{c}}},\ C^{\mathrm{a}}=\frac{1}{\nu^{\mathrm{a}}},\ \text{at the gate electrode}, \tag{C8a}$$

$$C^{\mathrm{h}}=C^{\mathrm{hD}}\ \text{at the drain electrode},\ C^{\mathrm{h}}=C^{\mathrm{h0}}\ \text{at the source electrode}, \tag{C8b}$$

$$(\mu^{\mathrm{s}})^{+}=(\mu^{\mathrm{s}})^{-},\ (\mu^{\mathrm{c}})^{+}=(\mu^{\mathrm{c}})^{-},\ \text{in } S_{\mathrm{OMIEC}}\cap S_{\mathrm{liquid}}, \tag{C8c}$$

$$N_K\left[J_K^{\mathrm{s}}(\boldsymbol{X},t)\right]^{\pm}=N_K\left[J_K^{\mathrm{c}}(\boldsymbol{X},t)\right]^{\pm}=N_K\left[J_K^{\mathrm{a}}(\boldsymbol{X},t)\right]^{\pm}=N_K\left[J_K^{\mathrm{h}}(\boldsymbol{X},t)\right]^{\pm}=0\ \text{on remaining boundaries}, \tag{C8d}$$

$$C^{\mathrm{s}} = \frac{1}{v^{\mathrm{s}}},\ C^{\mathrm{c}} = \frac{1}{v^{\mathrm{c}}},\ C^{\mathrm{a}} = \frac{1}{v^{\mathrm{a}}},\ \text{in } \Omega_{\mathrm{liquid}} \text{ at } t = 0, \tag{C8e}$$

$$C^{\mathrm{s}} = C^{\mathrm{sinit}},\ C^{\mathrm{c}} = C^{\mathrm{cinit}},\ C^{\mathrm{h}} = C^{\mathrm{hinit}},\ \text{in } \Omega_{\mathrm{OMIEC}} \text{ at } t = 0. \tag{C8f}$$

The governing equations for the electrical field solve the electrostatic potential V:

$$\frac{\partial \widetilde{D}_K(\boldsymbol{X},t)}{\partial X_K} = Q(\boldsymbol{X},t),\ \text{in } \Omega_{\mathrm{OMIEC}} \cup \Omega_{\mathrm{liquid}} \tag{C9a}$$

$$N_K[\widetilde{D}_K(\boldsymbol{X},t)]^{+} - N_K[\widetilde{D}_K(\boldsymbol{X},t)]^{-} = F\dot{j}^{\mathrm{h}}(\boldsymbol{X},t)\delta t,\ \text{in } S_{\mathrm{OMIEC}} \cup S_{\mathrm{liquid}} \tag{C9b}$$

where

$$\widetilde{E}_K = \frac{\partial W}{\partial \widetilde{D}_K} = -\frac{\partial V}{\partial X_K}, \tag{C10a}$$

$$D_i = \varepsilon E_i. \tag{C10b}$$

Specifically, we prescribed the following boundary and initial conditions in the model as shown in Fig. 3.

$$V = 0 \text{ at the source electrode,} \tag{C11a}$$

$$V = V_{\mathrm{G}} \text{ shown in Figure 7(a) at the gate electrode,} \tag{C11b}$$

$$V = -0.1\mathrm{V} \text{ at the drain electrode,} \tag{C11c}$$

$$V = 0 \text{ at } t = 0. \tag{C11d}$$

The governing equations for the phase field solve the phase parameter ϕ:

$$\dot{\phi} + \frac{\partial J_K^{\phi}(\boldsymbol{X},t)}{\partial X_K} = 0,\ \text{in } \Omega_{\mathrm{OMIEC}} \tag{C12a}$$

$$N_K\left[J_K^{\phi}(\boldsymbol{X},t)\right]^{+} - N_K\left[J_K^{\phi}(\boldsymbol{X},t)\right]^{-} = j^{\phi}(\boldsymbol{X},t),\ \text{in } S_{\mathrm{OMIEC}} \tag{C12b}$$

$$\begin{aligned} \mu^{\phi} \quad = \quad & \mu^{I,0} - \mu^{II,0} + RT\left[\frac{\ln\phi + 1}{N^{I}} - \frac{\ln(1-\phi)+1}{N^{II}} + \chi^{\phi}(1-2\phi)\right] + \frac{RTa^2}{36}\frac{(1-2\phi)}{\phi^2(1-\phi)^2}(\nabla\phi)^2 \\ & - \frac{4\Delta\gamma}{\rho^{\mathrm{sub}} d\left(1+\frac{X_2}{d}\right)^3} - RTa^2\left(\frac{\chi^{\phi}}{3} + \frac{1}{18\phi(1-\phi)}\right)\nabla^2\phi,\ \text{in } \Omega_{\mathrm{OMIEC}}, \end{aligned} \tag{C12c}$$

$$J_K^{\phi} = -\frac{C^{\phi}D^{\phi}}{RT}C_{KL}^{-1}\frac{\partial \mu^{\phi}}{\partial X_L},\ \text{in } \Omega_{\mathrm{OMIEC}}. \tag{C12d}$$

Specifically, we prescribed the following boundary and initial conditions in the model as shown in Fig. 3.

$$\phi = \mathrm{random}(X_1, X_2), \tag{C13a}$$

$$N_K\left[J_K^{\phi}(\boldsymbol{X},t)\right]^{\pm} = 0 \text{ on remaining boundaries,} \tag{C13b}$$

where the random function has two variables (X_1, X_2).

References

Anand, L., Aslan, O., Chester, S.A., 2012. A large-deformation gradient theory for elastic–plastic materials: strain softening and regularization of shear bands. Int. J. Plast. 30, 116–143.

Aerathupalathu Janardhanan, J., Chen, Y.L., Liu, C.T., Tseng, H.S., Wu, P.I., She, J.W., Hsiao, Y.S., Yu, H., 2022. Sensitive detection of sweat cortisol using an organic electrochemical transistor featuring nanostructured poly(3,4-ethylenedioxythiophene) derivatives in the channel layer. Anal. Chem. 94, 7584–7593.

Bießmann, L., Kreuzer, L.P., Widmann, T., Hohn, N., Moulin, J.F., Müller-Buschbaum, P., 2018. Monitoring the swelling behavior of PEDOT:PSS electrodes under high humidity conditions. ACS Appl. Mater. Interfaces 10, 9865–9872.

Bosnjak, N., Tepermeister, M., Silberstein, M.N., 2022. Modeling coupled electrochemical and mechanical behavior of soft ionic materials and ionotronic devices. J. Mech. Phys. Solids 168, 105014.

Cahn, J.W., 1965. Phase separation by spinodal decomposition in isotropic systems. J. Chem. Phys. 42, 93–99.

Cahn, J.W., Hilliard, J.E., 1958. Free energy of a nonuniform system. I. Interfacial free energy. J. Chem. Phys. 28, 258–267.
Cai, S., Suo, Z., 2011. Mechanics and chemical thermodynamics of phase transition in temperature-sensitive hydrogels. J. Mech. Phys. Solids 59, 2259–2278.
Celora, G.L., Hennessy, M.G., Münch, A., Wagner, B., Waters, S.L., 2022. A kinetic model of a polyelectrolyte gel undergoing phase separation. J. Mech. Phys. Solids 160, 104771.
Coleman, B.D., Noll, W., 1963. The thermodynamics of elastic materials with heat conduction and viscosity. Arch. Ration. Mech. Anal. 13 (1), 167–178.
Cruz-Cruz, I., Reyes-Reyes, M., Aguilar-Frutis, M.A., Rodriguez, A.G., López-Sandoval, R., 2010. Study of the effect of DMSO concentration on the thickness of the PSS insulating barrier in PEDOT:PSS thin films. Synth. Met. 160, 1501–1506.
Das, P., Zayat, B., Wei, Q., Salamat, C.Z., Magdău, I.B., Elizalde-Segovia, R., Rawlings, D., Lee, D., Pace, G., Irshad, A., Ye, L., Schmitt, A., Segalman, R.A., Miller, T.F., Tolbert, S.H., Dunn, B.S., Narayan, S.R., Thompson, B.C., 2020. Dihexyl-substituted poly(3,4-Propylenedioxythiophene) as a dual ionic and electronic conductive cathode binder for lithium-ion batteries. Chem. Mater. 32, 9176–9189.
Di Leo, C.V., Rejovitzky, E., Anand, L., 2015. Diffusion–deformation theory for amorphous silicon anodes: the role of plastic deformation on electrochemical performance. Int. J. Solids Struct. 67, 283–296.
Dingler, C., Walter, R., Gompf, B., Ludwigs, S., 2022. *In situ* monitoring of optical constants, conductivity, and swelling of PEDOT:PSS from doped to the fully neutral state. Macromolecules 55, 1600–1608.
Flory, P.J., 1942. Thermodynamics of high polymer solutions. J. Chem. Phys. 10, 51–61.
Flory, P.J., Rehner, J., 1943. Statistical mechanics of cross-linked polymer networks II. Swelling. J. Chem. Phys. 11, 521–526.
Gennes, PG.de, 1979. Scaling Concepts in Polymer Physics. Cornell University Press.
Gibbs, J.W., 1878. On the equilibrium of heterogeneous substances. Am. J. Sci. 441–458 s3-16.
Gkoupidenis, P., Schaefer, N., Garlan, B., Malliaras, G.G., 2015. Neuromorphic functions in PEDOT:PSS organic electrochemical transistors. Adv. Mater. 27, 7176–7180.
Go, G.T., Lee, Y., Seo, D.G., Lee, T.W., 2022. Organic Neuro-Electronics: from Neural Interface to Neuroprosthetics. Adv. Mater. 34 (45), 2201864.
Gueye, M.N., Carella, A., Faure-Vincent, J., Demadrille, R., Simonato, J.P., 2020. Progress in understanding structure and transport properties of PEDOT-based materials: a critical review. Prog. Mater. Sci 108, 100616.
Hidalgo Castillo, T.C., Moser, M., Cendra, C., Nayak, P.D., Salleo, A., McCulloch, I., Inal, S., 2022. Simultaneous performance and stability improvement of a p-type organic electrochemical transistor through additives. Chem. Mater. 34, 6723–6733.
Hong, W., Wang, X., 2013. A phase-field model for systems with coupled large deformation and mass transport. J. Mech. Phys. Solids 61, 1281–1294.
Hong, W., Zhao, X., Zhou, J., Suo, Z., 2008. A theory of coupled diffusion and large deformation in polymeric gels. J. Mech. Phys. Solids 56, 1779–1793.
Hong, W., Zhao, J., Suo, Z., 2010. Large deformation and electrochemistry of polyelectrolyte gels. J. Mech. Phys. Solids 58, 558–577.
Honma, Y., Itoh, K., Masunaga, H., Fujiwara, A., Nishizaki, T., Iguchi, S., Sasaki, T., 2018. Mesoscopic 2D charge transport in commonplace PEDOT:PSS films. Adv. Electron. Mater. 4, 1700490.
Kaphle, V., Paudel, P.R., Dahal, D., Radha Krishnan, R.K., Lüssem, B., 2020. Finding the equilibrium of organic electrochemical transistors. Nat. Commun. 11, 2515.
Kawahara, J., Ersman, P.A., Engquist, I., Berggren, M., 2012. Improving the color switch contrast in PEDOT:pSS-based electrochromic displays. Org. Electron. 13, 469–474.
Kayser, L.V., Lipomi, D.J., 2019. Stretchable conductive polymers and composites based on PEDOT and PEDOT:PSS. Adv. Mater. 31, 1806133.
Keene, S.T., Michaels, W., Melianas, A., Quill, T.J., Fuller, E.J., Giovannitti, A., McCulloch, I., Talin, A.A., Tassone, C.J., Qin, J., Troisi, A., Salleo, A., 2022. Efficient electronic tunneling governs transport in conducting polymer-insulator blends. J. Am. Chem. Soc. 144, 10368–10376.
Kim, J., Yin, T., Suo, Z., 2022. Polyacrylamide hydrogels. V. Some strands in a polymer network bear loads, but all strands contribute to swelling. J. Mech. Phys. Solids 168, 105017.
Kousseff, C.J., Halaksa, R., Parr, Z.S., Nielsen, C.B., 2022. Mixed ionic and electronic conduction in small-molecule semiconductors. Chem. Rev. 122, 4397–4419.
Lang, U., Naujoks, N., Dual, J., 2009. Mechanical characterization of PEDOT:PSS thin films. Synth. Met. 159, 473–479.
Li, X., Perera, K., He, J., Gumyusenge, A., Mei, J., 2019. Solution-processable electrochromic materials and devices: roadblocks and strategies towards large-scale applications. J. Mater. Chem. C 7, 12761–12789.
Liang, Y., Offenhäusser, A., Ingebrandt, S., Mayer, D., 2021. PEDOT:PSS-based bioelectronic devices for recording and modulation of electrophysiological and biochemical cell signals. Adv. Healthc. Mater. 10, 2100061.
Lubliner, J., 2008. Plasticity theory. Cour. Corp. 485.
Makki, H., Troisi, A., 2022. morphology of conducting polymer blends at the interface of conducting and insulating phases: insight from PEDOT: PSS atomistic simulations. J. Mater. Chem. C. 10 (42), 16126–16137.
Modarresi, M., Mehandzhiyski, A., Fahlman, M., Tybrandt, K., Zozoulenko, I., 2020. Microscopic understanding of the granular structure and the swelling of PEDOT: PSS. Macromolecules 53, 6267–6278.
Mozaffari, K., Liu, L., Sharma, P., 2022. Theory of soft solid electrolytes: overall properties of composite electrolytes, effect of deformation and microstructural design for enhanced ionic conductivity. J. Mech. Phys. Solids 158, 104621.
Nambiar, S., Yeow, J.T.W., 2011. Conductive polymer-based sensors for biomedical applications. Biosens. Bioelectron. 26, 1825–1832.
del Olmo, R., Mendes, T.C., Forsyth, M., Casado, N., 2022. Mixed ionic and electronic conducting binders containing PEDOT:PSS and organic ionic plastic crystals toward carbon-free solid-state battery cathodes. J. Mater. Chem. A.
Ouyang, L., Musumeci, C., Jafari, M.J., Ederth, T., Inganäs, O., 2015. Imaging the phase separation between PEDOT and polyelectrolytes during processing of highly conductive PEDOT:PSS films. ACS Appl. Mater. Interfaces 7, 19764–19773.
Palumbiny, C.M., Liu, F., Russell, T.P., Hexemer, A., Wang, C., Müller-Buschbaum, P., 2015. The crystallization of PEDOT:PSS polymeric electrodes probed *in situ* during printing. Adv. Mater. 27, 3391–3397.
Paulsen, B.D., Fabiano, S., Rivnay, J., 2021. Mixed ionic-electronic transport in polymers. Annu. Rev. Mater. Res. 51, 73–99.
Paulsen, B.D., Tybrandt, K., Stavrinidou, E., Rivnay, J., 2020. Organic mixed ionic–electronic conductors. Nat. Mater. 19, 13–26.
Picca, R.A., Manoli, K., Macchia, E., Sarcina, L., Di Franco, C., Cioffi, N., Blasi, D., Österbacka, R., Torricelli, F., Scamarcio, G., Torsi, L., 2020. Ultimately sensitive organic bioelectronic transistor sensors by materials and device structure design. Adv. Funct. Mater. 30, 1904513.
Rebetez, G., Bardagot, O., Affolter, J., Réhault, J., Banerji, N., 2022. What drives the kinetics and doping level in the electrochemical reactions of PEDOT:PSS? Adv. Funct. Mater. 32, 2105821.
Richards, R.W., Jones, R.A.L., 1999. Polymer/polymer interfaces. Polymers At Surfaces and Interfaces. Cambridge University Press, Cambridge, pp. 127–186.
Riess, I., 2000. Polymeric mixed ionic electronic conductors. Solid State Ionics. In: Proceedings of the 12th International Conference on Solid State Ionics 136–137, pp. 1119–1130.
Rivnay, J., Inal, S., Salleo, A., Owens, R.M., Berggren, M., Malliaras, G.G., 2018. Organic electrochemical transistors. Nat. Rev. Mater. 3, 1–14.
Saito, M., Yamada, N.L., Ito, K., Yokoyama, H., 2020. Interfacial energy measurement on the reconstructive polymer surface: dynamic polymer brush by segregation of amphiphilic block copolymers. Langmuir 36, 6465–6472.
Savva, A., Wustoni, S., Inal, S., 2018. Ionic-to-electronic coupling efficiency in PEDOT:PSS films operated in aqueous electrolytes. J. Mater. Chem. C 6, 12023–12030.
Shi, H., Liu, C., Jiang, Q., Xu, J., 2015. Effective approaches to improve the electrical conductivity of PEDOT:PSS: a review. Adv. Electron. Mater. 1, 1500017.
Shibayama, M., Tanaka, T., 1993. Volume phase transition and related phenomena of polymer gels. In: Dušek, K. (Ed.), Responsive gels: Volume transitions I, Advances in Polymer Science. Springer, Berlin, Heidelberg, pp. 1–62.
Simo, J.C., 1992. Algorithms for static and dynamic multiplicative plasticity that preserve the classical return mapping schemes of the infinitesimal theory. Comput. Methods in Appl. Mech. Eng. 99, 61–112.
Simo, J.C., Hughes, T.J.R., 2006. Computational Inelasticity. Springer Science & Business Media.
Szymański, M.Z., Tu, D., Forchheimer, R., 2017. 2-D Drift-diffusion simulation of organic electrochemical transistors. IEEE Trans. Electron Devices 64, 5114–5120.

Tan, S.T.M., Gumyusenge, A., Quill, T.J., LeCroy, G.S., Bonacchini, G.E., Denti, I., Salleo, A., 2022. Mixed ionic–electronic conduction, a multifunctional property in organic conductors. Adv. Mater. 34, 2110406.
Tanaka, T., Fillmore, D.J., 1979. Kinetics of swelling of gels. J. Chem. Phys. 70 (3), 1214–1218.
Tang, K., Miao, W., Guo, S., 2021. Crosslinked PEDOT:PSS organic electrochemical transistors on interdigitated electrodes with improved stability. ACS Appl. Polym. Mater. 3, 1436–1444.
Truesdell, C., Noll, W., 2004. The Non-Linear Field Theories of Mechanics. Springer, Berlin, Heidelberg.
Tybrandt, K., Zozoulenko, I.V., Berggren, M., 2017. Chemical potential–electric double layer coupling in conjugated polymer–polyelectrolyte blends. Sci. Adv. 3, eaao3659.
Velázquez Sánchez, M.M., 2002. Spinodal Decomposition in Thin Films of Binary Polymer Blends. Technische Universiteit Eindhoven.
Volkov, A.V., Wijeratne, K., Mitraka, E., Ail, U., Zhao, D., Tybrandt, K., Andreasen, J.W., Berggren, M., Crispin, X., Zozoulenko, I.V., 2017. Understanding the capacitance of PEDOT:PSS. Adv. Funct. Mater. 27, 1700329.
Wang, X., Chen, K., de Vasconcelos, L.S., He, J., Shin, Y.C., Mei, J., Zhao, K., 2020a. Mechanical breathing in organic electrochromics. Nat. Commun. 11, 211.
Wang, X., de Vasconcelos, L.S., Chen, K., Perera, K., Mei, J., Zhao, K., 2020b. *In situ* measurement of breathing strain and mechanical degradation in organic electrochromic polymers. ACS Appl. Mater. Interfaces 12, 50889–50895.
Wang, X., Li, X., Mei, J., Zhao, K., 2022. Doping kinetics in organic mixed ionic–electronic conductors: moving front experiments and the stress effect. Extreme Mech. Lett. 54, 101739.
Wang, X., Shapiro, B., Smela, E., 2009. Development of a model for charge transport in conjugated polymers. J. Phys. Chem. C 113, 382–401.
Xia, Y., Ouyang, J., 2012. Significant different conductivities of the two grades of poly(3,4-ethylenedioxythiophene):poly(styrenesulfonate), Clevios P and Clevios PH1000, arising from different molecular weights. ACS Appl. Mater. Interfaces 4, 4131–4140.
Xiao, Y., Bhattacharya, K., 2008. A continuum theory of deformable, semiconducting ferroelectrics. Arch. Ration. Mech. Anal. 189 (1), 59–95.
Yamamoto, S., Polyravas, A.G., Han, S., Malliaras, G.G., 2022. Correlation between transient response and neuromorphic behavior in organic electrochemical transistors. Adv. Electron. Mater. 8, 2101186.
Yeo, J.S., Yun, J.M., Kim, D.Y., Park, S., Kim, S.S., Yoon, M.H., Kim, T.W., Na, S.I., 2012. Significant vertical phase separation in solvent-vapor-annealed poly(3,4-ethylenedioxythiophene):poly(styrene sulfonate) composite films leading to better conductivity and work function for high-performance indium tin oxide-free optoelectronics. ACS Appl. Mater. Interfaces 4, 2551–2560.
Yildirim, E., Wu, G., Yong, X., Tan, T.L., Zhu, Q., Xu, J., Ouyang, J., Wang, J.S., Yang, S.W., 2018. A theoretical mechanistic study on electrical conductivity enhancement of DMSO treated PEDOT:PSS. J. Mater. Chem. C 6, 5122–5131.
Yu, Y., Landis, C.M., Huang, R., 2017. Salt-induced swelling and volume phase transition of polyelectrolyte gels. J. Appl. Mech. 84 (5), 051005.
Zhang, H., Dehghany, M., Hu, Y., 2020. Kinetics of polyelectrolyte gels. J. Appl. Mech. 87 (6), 061010.
Zhang, Y., van Doremaele, E.R.W., Ye, G., Stevens, T., Song, J., Chiechi, R.C., van de Burgt, Y., 2022. Adaptive biosensing and neuromorphic classification based on an ambipolar organic mixed ionic–electronic conductor. Adv. Mater. 34, 2200393.
Zhao, K., Pharr, M., Cai, S., Vlassak, J.J., Suo, Z., 2011. Large plastic deformation in high-capacity lithium-ion batteries caused by charge and discharge. J. Am. Ceram. Soc. 94, s226–s235.
Zhao, Y., Xu, B.X., Stein, P., Gross, D., 2016. Phase-field study of electrochemical reactions at exterior and interior interfaces in Li-ion battery electrode particles. Comput. Methods Appl. Mech. Eng. 312, 428–446.